

ALMA MATER STUDIORUM · UNIVERSITÀ DI
BOLOGNA

Scuola di Scienze
Dipartimento di Fisica e Astronomia
Corso di Laurea Magistrale in Fisica

Proton-induced cross sections on ^{nat}V
target: focus on ^{47}Sc production

Relatore:
Prof. Mauro Bruno

Presentata da:
Lucia De Dominicis

Correlatrici:
Dott.ssa Gaia Pupillo
Dott.ssa Liliana Mou

Anno Accademico 2018/2019

Abstract

Il gruppo NUCL-EX si interessa a misure di sezioni d'urto di produzione di isotopi instabili selezionati, presso i Laboratori Nazionali di Legnaro appartenenti all'Istituto Nazionale di Fisica Nucleare (INFN-LNL). Poiché il progetto SPES, il futuro dei LNL, è attualmente in fase di costruzione, si è creata una collaborazione con il gruppo LARAMED, operante nel campo della produzione di radionuclidi con applicazione medica. In particolare, questa tesi è incentrata sull'analisi dei dati sperimentali nell'ambito delle misure di sezioni d'urto, indotte da protoni, di interesse sia in fisica nucleare che interdisciplinare. Il lavoro realizzato e presentato in questa tesi rientra nel contesto del progetto PASTA (Production with Accelerator of SC-47 for Theranostic Applications), il cui scopo è lo studio della produzione dello ^{47}Sc e dei suoi contaminanti, tutti prodotti mediante reazioni nucleari indotte da un fascio di protoni, di energia variabile, su un bersaglio di ^{nat}V . L'interesse nello ^{47}Sc è motivato dalla sua promettente applicazione in campo medico, in particolare nella teragnostica, un nuovo approccio alla medicina che sfrutta le radiazioni emesse (γ e β^-) sia per la terapia che per la diagnosi, indirizzata alla cura dei tumori. Dato che per tali applicazioni è richiesto un livello di purezza elevato per lo ^{47}Sc prodotto, in questo lavoro sono state misurate (e sono presentate) anche le sezioni d'urto di produzione di tutti i radionuclidi contaminanti. Tra essi il più problematico è lo ^{46}Sc dato che, essendo un altro isotopo dello scandio, non può essere separato chimicamente e, poiché la sua vita media è più lunga di quella dello ^{47}Sc , non è possibile aspettare che decada. Lo scopo di questa tesi è di trovare un intervallo di energia, se possibile, in cui lo ^{47}Sc ha un valore di sezione d'urto più alto di quello che si ha per lo ^{46}Sc . Tale intervallo potrebbe essere sfruttato per produrre ^{47}Sc sufficientemente puro da poter essere utilizzato in futuri studi preclinici che ne testino l'efficacia terapeutica.

Abstract

The NUCL-EX team has the project of working on cross section measurements for the production of stable and radioactive selected nuclei at the Legnaro National Laboratories of the National Institute of Nuclear Physics (INFN-LNL). Considering that the SPES project, the future of LNL, is nowadays under construction, a collaboration is created with the LARAMED team, that is working in the field of radioisotopes production with medical application. In particular, this thesis is focused on the analysis of experimental data obtained on cross section measurements, induced by proton beams, for the production of radionuclides of interest both in nuclear and in interdisciplinary physics. The work realized and presented in this thesis is part of the PASTA project (Production with Accelerator of Sc-47 for Theranostic Applications), whose aim is the study of ^{47}Sc production by using accelerators. The thesis' work is focused on the measurement of the nuclear cross section to produce ^{47}Sc and contaminants, i.e. all the radionuclides co-produced during the bombardment of the natV targets with the proton beams of various energy. The interest on ^{47}Sc is due to its promising application in medicine, especially in theranostics, the new approach in cancer treatment that exploits the emitted radiation (γ and β^-), useful for both diagnosis and therapy. Since a highly pure product is required in this kind of applications, this work considers not only the ^{47}Sc production but also the cross sections of all the co-produced contaminants. Among them, the one requiring particular attention is ^{46}Sc since, as all Sc-isotopes, can not be chemically separated from ^{47}Sc and, considering its longer half-life than ^{47}Sc , can not be removed by waiting a proper decay time. The aim of this thesis is to find out, if possible, an optimal energy range where the cross section for ^{47}Sc production is higher than the one of ^{46}Sc . Such energy interval might be exploited to produce ^{47}Sc with acceptable purity to use it for preclinical studies aimed at testing its therapeutic efficacy.

Contents

Introduction	3
1 Scandium for theranostics applications	6
1.1 The diagnostic aspect of theranostics: PET and SPECT . . .	7
1.2 The therapeutic aspect of theranostics: the promising ^{47}Sc . .	9
1.3 State of the art of ^{47}Sc production	10
2 Radioactive nuclei	12
2.1 Radioisotopes production	12
2.2 Production cross sections	14
2.3 Radioactive decay	15
2.3.1 Alpha decay	15
2.3.2 Beta decay	16
2.3.3 Gamma decay	17
2.3.4 Radioactive decay law	18
2.4 Interaction of photons in matter	19
2.4.1 Photoelectric effect	19
2.4.2 Compton scattering	21
2.4.3 Pair production	24
2.4.4 Photons total cross section	25
2.5 Typical features of γ -spectra	27
3 Instruments for cross sections measurements	32
3.1 Cyclotron accelerators	32
3.2 LNL future cyclotron and facility	34
3.3 The ARRONAX cyclotron	37
3.4 Stacked-foils target assembling	38
3.5 Semiconductor detectors	41
3.6 The HPGe detector at ARRONAX facility	45

4	Determination of the cross sections to produce radionuclides of medical interest	47
4.1	The acquisition data procedure	48
4.2	Analysis operations	49
4.2.1	The case of ^{44m}Sc and ^{44g}Sc	53
4.3	Calculation of the cross section energy values	54
5	Presentation of the results	56
5.1	Cross sections of all the radionuclides produced by $^{nat}\text{V}(\text{p},\text{x})$ reactions	56
5.1.1	^{48}Cr production	57
5.1.2	^{49}Cr production	57
5.1.3	^{51}Cr production	58
5.1.4	^{48}V production	61
5.1.5	^{43}Sc production	63
5.1.6	^{44m}Sc production	64
5.1.7	^{44g}Sc production	65
5.1.8	^{46}Sc production	66
5.1.9	^{47}Sc production	68
5.1.10	^{48}Sc production	71
5.1.11	^{42}K production	73
5.1.12	^{43}K production	73
5.2	Comparison of the experimental results with the previous data	75
	Conclusions	85
	Appendix A: IAEA monitor reactions	87
	Appendix B: $^{nat}\text{V}(\text{p},\text{x})$ reactions	89

Introduction

Nuclear medicine originated with the birth of the first cyclotron, ideated by Ernest Lawrence. The Ernest objective was to accelerate particles enough to achieve sufficiently high energies to produce new particles when bombarding a target. It was his brother, John Lawrence, who thought of the implication that a cyclotron could have in medicine field. He realized that radioisotopes generated by the cyclotron could be used to treat cancer. This innovative idea led, nowadays, to hundreds of different kinds of procedures involving radioisotopes for both diagnosis and therapy of several conditions nowadays.

Considering the great success that the employment of radionuclides has achieved, the IAEA (International Atomic Energy Agency) expressed the need to increase worldwide capacity of radioisotopes production and distribution, as well as to investigate the possibility to introduce new emerging radionuclides in the routine procedures in hospitals. To stimulate this progress, the IAEA promoted a Coordinated Research Project (CRP) [1].

In this context took hold the LARAMED (LABoratory of RADioisotopes for MEDicine) project [2], aimed to produce different radioisotopes of medical interest. It is a project funded by the MIUR (Ministero Italiano per l'Università e la Ricerca) and INFN (Istituto Nazionale di Fisica Nucleare). LARAMED can rely on the high performance 70p cyclotron, installed in 2015 at LNL (Laboratori Nazionali di Legnaro), one of the four italian laboratories belonging to INFN, and commissioned within the broader framework of SPES (Selective Production of Exotic Species) [3]. The cyclotron installed is able to extract two beam lines simultaneously, reflecting the dual purposes of the SPES project. In fact, SPES goals regard both fundamental research activities in nuclear physics and astrophysics and on interdisciplinary applications, ranging from the production of radionuclides of medical interest to the generation of neutrons for material studies and nuclear technologies. The RILAB (RadioIsotopes LABoratory) bunkers for LARAMED experimental activities will include two beam lines. One is devoted to cross section measurements (maximum beam current 100 nA), the other to the production of radionuclides for preclinical studies, carried out in collaboration with

external research institutes, such as the IOV (Istituto Oncologico Veneto). Nowadays, the beam lines are under installation and the research activities of the LARAMED project are performed in collaboration with the ARRONAX facility (Nantes, France), the Sacro Cuore Don Calabria hospital (Negrar, Verona, Italy) and the University of Ferrara (Ferrara, Italy).

In these years, several radionuclides have been investigated (^{99m}Tc , ^{99}Mo , ^{67}Cu , ^{51}Mn , ^{52}Mn), in the framework of dedicated projects funded by INFN. In 2017 and 2018 the research activities were focused on ^{47}Sc with the PASTA project, acronym of Production with Accelerators of ^{47}Sc for Theranostic Applications (Bando INFN per Giovani Ricercatrici e Ricercatori No. 18203). The interest on ^{47}Sc , suggested as emerging theranostic radionuclide by the CRP promoted by IAEA [1], is also due to the possibility to pair it with other Scandium isotopes β^+ emitters, like ^{44}Sc and ^{43}Sc . The use of radiopharmaceuticals, labelled with different scandium isotopes that have identical chemical properties, is the possibility to perform diagnosis prior therapy, by using the same molecule. This theranostic approach allows the selection of patients who positively respond to the radiopharmaceutical. Moreover, the use of β^+ emitters and PET screenings permit to tailor the dose to specific patients' needs, a further step towards personalized medicine.

^{47}Sc , in addition to β^- emission, exploited to treat small to medium sized tumors through the delivery of cytotoxic levels of radiations to insane cells, has also a γ -emission, suitable to monitor the tumor uptake through SPECT imaging, as discussed in Chapter 1. The fundamental physics regarding the radionuclides production and the description of the different decay modes is presented in the Chapter 2. Chapter 3 presents all the necessary instruments used to measure nuclear cross sections. As previously reported, since the LARAMED facility and laboratories are currently under construction, the experiments of the PASTA project were carried out at the ARRONAX facility (Nantes, France) [4]. Different spectra are available for the analysis after the irradiation runs. Starting from those spectra, the cross section measures should be derived. The formulas and the procedure followed to obtain the cross section values for all the isotopes produced in reactions induced by proton beams on ^{nat}V targets are exposed in Chapter 4. Even if ^{47}Sc is the radioisotope of interest, the cross section of all the radionuclides during the irradiation are calculated, since they may affect the purity of the final product. Most of the co-produced contaminants can be easily removed through a proper chemical separation. Sc-isotopes, instead, have all the same chemical properties: for this reason, only a proper cooling time can be applied to let the shorter-lived isotopes decay. The main issue is the ^{46}Sc ($T_{1/2}=83.79$ d) production, since it has an half-life longer than ^{47}Sc ($T_{1/2}=3.3492$ h). The solution is to identify an energy range in which ^{47}Sc is produced while ^{46}Sc

is not. To do this the results presented in Chapter 5 are necessary. Also the NUCL-EX group is interested in those results in view of a future collaboration on cross section measurements.

In conclusion, the aim of my thesis work is to evaluate the possibility to produce the theranostic ^{47}Sc through the irradiation of ^{nat}V targets with a proton beam provided by a cyclotron.

Chapter 1

Scandium for theranostics applications

An important challenge of nuclear medicine is to find new techniques able to provide effective cancer diagnostics and treatment at the very early stages of the disease [5]. To achieve this goal, a new rapidly growing field in nuclear medicine is radionuclide therapy. This method is based on the concept of delivering cytotoxic levels of radiation to disease sites, with the advantage of hitting the disease at the cellular level rather than at anatomical level, avoiding a surgical invasive procedure. Another aspect of radionuclide therapy is its ability to perform molecular imaging studies to determine the selective accumulation in the treated tissue, using Single Photon Emission Computed Tomography (SPECT) or Positron Emission Tomography (PET). This application of nuclear medicine requires the use of radiopharmaceuticals, pharmaceutical drugs containing one or more radioactive nuclides, to investigate different kinds of diseases and to treat tumors. Radiopharmaceuticals, in fact, are the base of molecular imaging, providing pictures of what is happening inside the body at the molecular and cellular level with the aim to study specific biological processes [6]. The use of radiopharmaceuticals to combine the imaging techniques for diagnosis with the ability of efficiently targeting the cell of interest for therapy is called theranostics. Theranostics exploits a combination of therapeutic emissions, such as alpha, beta or Auger ('thera'), and diagnostic emissions, such as gamma or positrons ('nostic'). The key advantages of the theranostics include the personalization of therapy based on uptake of the lower-dose diagnostic. This highly personalized approach should allow a better treatment efficiency for the patient and a lower social economic cost [5]. This means that it is possible to:

- select patients that respond to a given treatment and consequently

optimize the treatment for each patient;

- verify the staging of the disease;
- perform dosimetric calculations to tailor the therapeutic dose, optimizing the radioactivity value to inject;
- check the efficiency of the treatment with a diagnostic procedure after a proper time from the administration of the therapeutic dose.

To perform theranostic procedures three different radionuclides combinations are possible. First of all there is the multiple-element theranostics: in this method different elements showing similar chemical properties can be used with the same targeting molecule. For example ^{188}Re ($T_{1/2}=17.005$ h, $E_{\beta^-}=763$ keV) and ^{99m}Tc ($T_{1/2}=6.0072$ h, $E_{\gamma}=140.511$ keV) are used together for diagnosis and therapy. Then also single-element theranostics is possible: this involves different isotopes of the same element, each emitting therapeutic or diagnostic particles. ^{43}Sc ($T_{1/2}=3.891$ h, $E_{\beta^+}=476$ keV) or ^{44}Sc ($T_{1/2}=3.97$ h, $E_{\beta^+}=632.0$ keV) can be associated to ^{47}Sc ($T_{1/2}=3.3492$ h, $E_{\beta^-}=162.0$ keV). In the end, can be used the single-radionuclide theranostics: here a single radioisotope serves as theranostic radionuclide producing both diagnostic and therapeutic radiations. In this case, ^{47}Sc and ^{67}Cu are suitable for SPECT imaging and therapy for example, or, alternatively, ^{64}Cu can provide PET imaging and therapy.

In its continuous effort to stimulate progress in medical applications of radionuclides, the IAEA has promoted a number of programs aimed at ensuring a wider availability of important medical radionuclides in Member States. Of particular interest are the emerging radionuclides that have already demonstrated to have high potential for application in cancer therapy. For this purpose a Coordinated Research Project (CRP) started in 2016, focused on the development of radiopharmaceuticals labelled with these new radionuclides [1]. Among these new radionuclides ^{47}Sc is mentioned as emerging promising theranostic radionuclide.

1.1 The diagnostic aspect of theranostics: PET and SPECT

All the radionuclides involved in diagnostic procedures should emit one between:

- γ -rays, directly during the decay, suitable for Single Photon Emission Computed Tomography (SPECT);

- β^+ particles, which subsequently undergoes annihilation with an electron, producing two γ -rays at 511 keV each, exploitable for Positron Emission Tomography (PET).

PET and SPECT are the basis of nuclear medicine imaging tools and play an important role, surely in early diagnosis, but also in prognosis and monitoring of progress, regression or stagnation of a disease previously treated with a specific therapy.

SPECT is a cornerstone of nuclear medicine: it is mainly used for the detection of molecular changes in cardiovascular, neurological and oncological diseases. The operating principle is well known from 1980s and it consists in injecting in the patient a bioactive molecule or a radiopharmaceutical, labelled with a γ -ray emitter radionuclide, in the patient. Then, with a camera designed for SPECT imaging, generally a scintillator connected to PMTs (Photo-Multiplier Tubes), the outgoing γ -rays are detected. The emitted radiation should have energy not too high, in order to be detected in medium-size crystals, but not too low because it should be able to come out from the body of the patient. In order to reduce the dose delivered to the patient as much as possible, the ideal radionuclide should emit only the radiation of interest.

Nowadays, although different radionuclides are available as tracers, ^{99m}Tc is still the most common SPECT radionuclide, constituting around the 90% of the over 30 million procedures, based on radioisotopes compounds, performed per year worldwide.

PET exploits radiopharmaceuticals labelled with radionuclides emitting β^+ particles, so the working principle is the same of SPECT but, instead of a single photon, the PET-cameras have to detect two quasi-opposite 511 keV γ -rays. The most used radionuclide in PET diagnosis is ^{18}F ($T_{1/2}=109.77$ min, $E_{\beta^+}=249.8$ keV) but also ^{11}C ($T_{1/2}=20.364$ min, $E_{\beta^+}=385.7$ keV), ^{13}N ($T_{1/2}=9.965$ min, $E_{\beta^+}=491.82$ keV) and ^{68}Ga ($T_{1/2}=67.71$ min, $E_{\beta^+}=829.5$ keV) are used.

In general, the radionuclides employed for diagnostic procedures should:

- have a half-life long enough to allow the radiopharmaceutical preparation but short enough to minimize the absorbed patient dose (in general less than 24 h);
- emit only low energy γ -rays or β^+ particles which are compatible with SPECT and PET imaging respectively;
- have robust chemistry and chemical properties suitable to synthesize radiopharmaceuticals with high radiochemical yields and particularly stable in vivo.

Among the radionuclides that show decay characteristics similar to those listed there are metals. In particular, transition metals such as ^{99m}Tc have rich coordination chemistry, allowing links with different ligands in radiochemical preparations [6].

There is also Scandium, evaluated as a new promising theranostic radionuclide. Some of its isotopes are useful in the diagnosis phase. ^{43}Sc is a β^+ emitting radioisotope used for PET imaging, with similar properties to ^{44}Sc . ^{44}Sc is also used in PET diagnosis. Its peculiarity is the possible coproduction of the metastable state ^{44m}Sc ($T_{1/2}=58.61$ h, $E_\gamma=271.241$ keV). When ^{44m}Sc decays to the ground state there are no changes in the oxidation state, so the labelling properties of the compound should be maintained. This indicates that $^{44m}\text{Sc}/^{44}\text{Sc}$ can be used as an *in vivo* generator, since the effective half-life of ^{44}Sc can be increased, and, as a consequence, that it can be associated with large vectors, such as antibodies, which require long time to distribute within the body [7]. Moreover, few nanoseconds after β^+ -decay, ^{44}Sc also emits a γ at 1157 keV in 99.9% of the cases. This characteristic is proposed to be used in a new nuclear medical imaging technique based on measurement of emitter position, detecting the three photons in coincidence (one γ and two annihilation photons) [8].

Both ^{43}Sc and ^{44}Sc have a half-life of about 4 h, making them compatible with the pharmacokinetics of a wide range of targeting vectors, such as peptides and antibody fragments. In fact the use of those vectors is limited because of the short half-life of commonly used PET radionuclides. Their longer half-lives, if compared to the currently employed ^{68}Ga , allows also the shipment of radiopharmaceuticals labelled with ^{43}Sc or ^{44}Sc to distant PET centers [9]. In addition, images can be acquired over long period. At the end of their half-lives, ^{43}Sc and ^{44}Sc decay in Ca isotopes which are nontoxic for human body.

^{47}Sc , on the other hand, follows a β^- decay but also emits a primary γ -ray at an energy of 159.381 keV, which is similar to that of ^{99m}Tc , and that makes it ideal for SPECT imaging also with the same cameras designed for imaging with ^{99m}Tc .

1.2 The therapeutic aspect of theranostics: the promising ^{47}Sc

Nuclides having β^- , α or Auger electrons emissions can be employed in nuclear medicine to perform therapeutic treatments of tumors, considering their ability to destroy cells, responsible for pathologies, through the biological

effect of emitted radiation. In particular, α particles produce very high-localized ionization densities in cells. Their short range in tissues make them perfect for treating small tumors. Auger electrons are electrons with very low energy and very short range. The range is so short that can be defined a subcellular range, so it is important that Auger emitting radionuclides are deposited within or extremely close to the nucleus of the cells for maximum effectiveness. β^- particles can be used for small tumors treatment if they have low to medium energy, or can be used in the therapy of larger tumors when their energy is higher.

In general several factors should be taken into consideration in choosing a particular radioisotope for therapy, such as half-life, energy of particles emitted, type of particle emitted and the cost and availability of the radioisotope. They are mostly in common with diagnostic radionuclide characteristics. The half-life, in fact, must match the pharmacokinetics of the radioactive drug, specifically for uptake and clearance from normal versus targeted tissues, in order to maximize the dose to the target and minimize the one to normal tissues.

^{47}Sc is a β^- emitter with low to moderate beta energies. The advantage that makes ^{47}Sc attractive is its chemical similarity to ^{177}Lu ($T_{1/2}=6.647$ d, $E_{\beta^-}=134.2$ keV) and ^{90}Y ($T_{1/2}=64.00$ h, $E_{\beta^-}=933.6$ keV), which are the radionuclides actually widely used in targeted therapy. This characteristic allows to use the same ligands, just developed for the previous employed radionuclides, also for ^{47}Sc , so they don't imply the creation of new radiopharmaceuticals. One more positive aspect is that ^{47}Sc can be potentially produced in cyclotrons, while ^{177}Lu is produced only in nuclear reactors.

In conclusion, it is clear that ^{47}Sc seems to be a really interesting radionuclide usable as exclusively therapeutic radioisotope, paired with other Sc diagnostic isotopes to perform theranostics, or directly as theranostic radionuclide itself alone. This makes ^{47}Sc more appealing given that, in this way, it is enabled the concept of using chemically identical radiopharmaceuticals with the same kinetic properties for diagnosis and therapy.

1.3 State of the art of ^{47}Sc production

While convenient ways of ^{43}Sc and ^{44}Sc production are identified and ^{44}Sc applications are quite extensively studied, ^{47}Sc remains poorly scrutinized [7]. Different production possibilities were proposed for ^{47}Sc , but none of them is evaluated as the most suitable so far. All of them involve charged particles irradiating a target formed by Ca or Ti isotopes. The limitations from one pathway to another are mainly due to impurities. ^{46}Sc long half-

life ($T_{1/2}=83.79$ d) makes it the inevitable co-production contaminant in the case of ^{47}Sc , problematic for a medical use. Another possible limitation can be the starting enriched material availability, used for the target, associated to an efficient and simple separation chemistry.

So the challenge is still finding a favorable production method when considering aspects as purity and target availability. In the framework of the LARAMED program at INFN-LNL, the PASTA project aims to study production mechanisms of ^{47}Sc , such as reaction channels, cross sections and contaminants, starting from ^{nat}V as a target. The idea is to irradiate a ^{nat}V target with a proton beam of tunable energy, in the range from 26 MeV to 70 MeV, to exploit the reaction $^{nat}\text{V}(p,x)^{47}\text{Sc}$. The advantages of using ^{nat}V as a target are the availability at low cost, since it can be used with its natural abundances and does not need any enrichment, and the simple needed chemical separation after irradiation. On the other hand, when using ^{nat}V , the co-produced contaminant ^{46}Sc is present. To reduce this problem also the contaminant cross section is studied to determine an energy range in which the ^{46}Sc is null or sufficiently low. After the consideration of all these aspects, ^{nat}V can be seriously taken into consideration as an alternative way to produce ^{47}Sc theranostic radioisotope.

Chapter 2

Radioactive nuclei

A nucleus in an atom contains a certain number of protons and neutrons and its stability is the result of the balance between two forces: the electric repulsion between protons, which are all positively charged, and the strong force acting over small distances in the nucleus. For a given number of protons, the number of neutrons can vary determining the existence of isotopes for each atom. Some of those isotopes are stable while others are unstable due to an excess of either protons or neutrons. The unstable ones statistically decay in a more stable configuration after a given interval of time, emitting radiation and generating a new atom. For this reason they are called radioactive isotopes or nuclei.

The majority of nuclei in the environment are stable so they don't decay over time. This is because almost all natural unstable nuclei have just decayed and vanished. The only unstable nuclei still present are those with a long lifetime, like Uranium and Thorium, their radioactive decay chains products and those which are continuously regenerated by cosmic rays. In 1934 Irène and Frédéric Joliot-Curie produced the first radioactive nucleus of phosphorus bombarding a sheet of aluminium with alpha particles. From that moment a large number of radioactive isotopes started to be created artificially.

2.1 Radioisotopes production

There are two main procedures for the production of radioisotopes for medical applications: the exposure of a target to neutrons coming from research reactors and the bombardment with a beam, composed by charged particles or photons, produced by accelerators. Those two methods are complementary and together offer a large set of radioactive isotopes.

In nuclear reactors the production of radioactive nuclei is based on the

process of neutron capture that takes place in the target material. Alternatively, neutrons from the reactor core can trigger the fission of ^{235}U in the target. With reactors a large variety of radionuclides can be produced. For example, ^{99}Mo and its daughter $^{99\text{m}}\text{Tc}$ provide the 80% of the radioisotopes employed in diagnostic procedures worldwide and they are at the moment completely produced in research reactors [10] for economical reasons.

The positive aspect of using cyclotrons is that they can be installed directly in industrial sites or hospitals allowing a more immediate use of radionuclides. Moreover, cyclotrons have more compact dimensions and there are several worldwide companies able to supply them. Since the proton-induced reactions are the most employed for radioisotopes production, cyclotrons are the predominant choice for this purpose. The proton energies required are in most cases moderate. PET isotopes can be produced already between 11-19 MeV, while SPECT ones require 30 MeV protons. In figure 2.1 is possible to notice which was the number of cyclotrons in operation for radioisotopes production at different proton energy ranges worldwide in 2013 for [8]. Cyclotrons can accelerate also charged ions, such as deuterons, ^3He

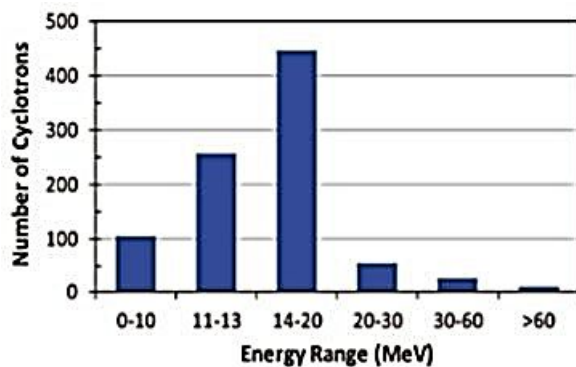


Figure 2.1: Worldwide number of cyclotrons as a function of their maximum proton energy in 2013 [8].

and ^4He , but with reduced efficiency.

Another contribution is given by linear accelerators for example when the proton energies needed are higher than that available at standard medical cyclotrons.

When accelerated protons interact with nuclei of the target material, different nuclear reactions can occur, depending on the energy of the incident particle. The effect of such interaction is the production of new nuclear species (stable or radioactive) and the emission of protons, neutrons or other nuclear fragments. The production of radionuclides surely depends on the target material and its composition, but also on the incident beam energy, the

target thickness, which determine the outgoing beam energy, and the irradiation time. The key element to properly find the best irradiation conditions is the accurate knowledge of the production cross sections of the radionuclide of interest and related contaminants. In fact, the cross section indicates the probability that a certain nuclear reaction occurs, in dependence of the beam energy. As the energy of the incident particles increases, also the number of possible reaction channels increases, and accordingly the radionuclide species that can be produced. In particular, at lowest energies (5-15 MeV), the (p,n) and (p, α) reactions are the dominant ones. Those are the main processes needed to produce PET radioisotopes. As the proton energy grows, new channels are opened such as (p,2n), (p,3n) and (p,4n). For example 30 MeV protons allow the use of (p,2n) reactions while at 70 MeV the (p,4n) reactions are possible. Tens of MeV are also necessary to exploit the reaction (p,2p). At even higher energies the scenario becomes more complicated. Energies of 100 MeV or more induce spallation processes, making the variety of products more wider.

It should be taken into account that in most cases each radioisotope can be obtained through different reactions in which are changed not only the projectile energy and the target material composition, but also the mass and the charge of the projectile. However, the choice of protons is often based also on practical aspects, such as the large availability of medium-small sized proton cyclotrons, as shown in figure 2.1. In fact the majority of radionuclides used in diagnostic medicine are efficiently produced with proton accelerators.

2.2 Production cross sections

The presence and the amount of a nucleus among the final products is described by the value of the specific cross section at the energy selected for the bombarding beam. So the production cross section represents the probability that a proton of given energy arriving on the target interacts with a nucleus in that target to generate a selected isotope. The symbol of the cross section is σ and is measured in barns. For each isotope σ is usually graphed in function of the projectile energy.

The knowledge of the production cross sections for medical radionuclides is important to derive which is the optimal beam energy to set during production sessions, but also the production cross section of all the other radioactive nuclei have to be known because they can have side effects during the medical procedure. For this reason, the study of the production cross sections of all the radioisotopes generated during an irradiation is a key point of this work. For example, it is possible that the best energy range to pro-

duce a specific radionuclide does not correspond to the interval where its cross section is maximized. In fact, often the optimal energy range partially covers the interval where the cross section of the radionuclide of interest is at maximum, in order to avoid the co-production of specific contaminants. The key word to find the best balance in this optimization process is "purity". A pure product is the one in which there are no other radioisotopes in addition to the desired one. Obviously it is quite demanding, but some expedient may help. For example, the primary method comes from the chemical separation, that is able to select and isolate a specific chemical specie from the irradiated material. In addition to the extraction step, a radiochemical process is also able to purify the desired product from all the other co-produced contaminants. This technique allows to split the different species taking advantage of the different chemical properties they show, but it is ineffective when the impurity is another isotope of the same element. Sometimes the decay times can be exploited to solve the latter problem. It is the case when the decay time of the impurity is considerably shorter than the desired radionuclide, in this way waiting a reasonable cooling time the activity of the contaminants can be reduced to a proper value.

Cases in which previous methods are unusefull require the evaluation of cross sections to estimate the inevitable amount of contaminative radiation and select, if possible, an advantageous energy range in which that presence is within certain limits. Generally, low energy projectiles have at disposal few reaction channels that means higher probability to have less impurities. As a consequence higher energies, even if may increase the production yield, bring to a wider set of products [5].

The aim of this work is indeed to present the production cross sections of all the radionuclides resulting from the bombardment of a natural Vanadium target with protons of energies in the range from 26 MeV to 70 MeV.

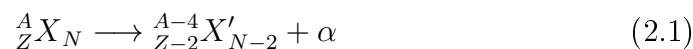
2.3 Radioactive decay

To determine if a radioisotope is produced during bombardment, it is necessary to find a way to detect it. Since radioactive nuclei are unstable their decay can provide detectable objects. There are three decay ways, called alpha, beta and gamma, from the first three letters of the Greek alphabet.

2.3.1 Alpha decay

An α particle is constituted by two protons and two neutrons bound together, so it is another way to name the helium nucleus. The emission of alpha

particles is an effect of Coulomb repulsion and so it is typical of heaviest nuclei. The Coulomb force is proportional to Z^2 (atomic number, number of protons or electrons) so it fast increases with nuclei size. Moreover, the Coulomb force depending on Z , is stronger than that of the binding force, which is approximately linear with A (atomic mass, number of protons plus number of neutrons). As a result, in heavier elements the Coulomb repulsion dominates on nuclear bounds and an helium nucleus is emitted to reach a more stable configuration. The process is described as

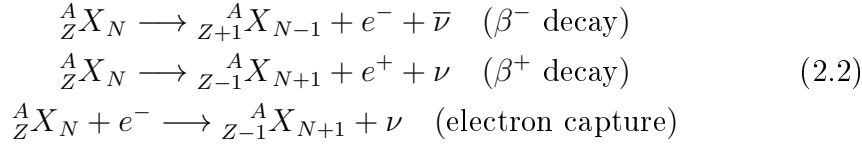


From equation 2.1 the result of the process is that the original atom is changed into a different element with its atomic number decreased of 2 units while the mass number decreased of 4. It is easy to understand that between the two opposite forces is the Coulomb one that undergoes a more significant attenuation.

Once the alpha particle is emitted, it is immediately repelled from the nucleus because are both positively charged. The energy released is asymmetrically shared between the α and the transformed nucleus, due to their different masses. The alpha particle receives about 98% of the total available energy while the recoil nucleus takes the rest.

2.3.2 Beta decay

This type of radiation is governed by a force able to convert a nucleon into the other, so to transform a proton into a neutron or a neutron into a proton. This force is the weak force. The result of the decay is the change of the atomic number Z of 1 unit while the total number of nucleons, given by A , remains the same. The transformation process is supported by the emission of an electron or a positron, the β particle, to fulfill the charge conservation. The observations at the beginning of 1920s showed that the dynamic wasn't complete in this configuration because the beta particle has a continuous energy distribution. The expectation was that for the same reaction the electrons or positrons emitted should have always the same value of energy. This prediction was obviously unsatisfied. In 1931 Pauli suggested that could exist a one more elusive particle with which the β particle shares the kinetic energy of the final state. This particle was called neutrino by Fermi. At this point the clear dynamic for the three different types of beta decay can be represented by



In this way the energy released in β^+ and β^- decay is divided between three elements: the recoil nucleus, the electron (or positron) and the antineutrino (or neutrino). The nucleus, which has the greatest mass, takes away a small portion of the energy. So the two light particles share almost all the available energy and the electron (or positron) usually picks up on average a little less than half of it. Between the two beta decays the β^- emitters are more common than β^+ ones because a proton excess is rarest in nature.

Concerning the last possible process, the electron capture, it is the less frequent. It consists in the capture of one of the orbital electrons by the nucleus, which consequently transforms one of its protons into a neutron, emitting a neutrino. The electrons orbit on average at a distance larger than the action range of weak force, for this reason the electron capture is so rare even if is energetically favored compared to its competitor β^+ decay, which requires an energy threshold equal to the positron mass.

In conclusion the β^- decay occur in neutron-rich nuclei, while β^+ decay and electron capture are useful to reduce the number of protons. Those reactions are usually observed in nature in radionuclides with a half-life shorter than that of alpha emitters. Furthermore, the energies of beta particles are smaller than those of alpha particles, ranging from few keV to 1 MeV while α are above 4 MeV.

2.3.3 Gamma decay

Nearly always α and β decays leave the nucleus in an excited state. These excited states have an excess of energy and so rapidly decay to the ground state emitting one or more γ -rays, which take away this extra energy. The interval of possible gamma energies ranges between 0.1 MeV and 10 MeV. The process can be seen as the de-excitation of the nucleus that usually occur in an atom but transposed in the nucleus. In parallel with the atom, the nucleus has defined energy states. The motion from an energy level to another is characterized by the emission of a gamma ray of specific energy given by the transition performed and the type of nucleus involved. From this point of view, knowing the energy of the gamma, is possible to identify which is the emitting. For this reason, sometimes the emitted gamma-rays are mentioned as the fingerprints of the nuclei.

The gamma emission is almost always instantaneous with some exceptions in which the emission is delayed. This is the case of the excited state of the Technetium that lasts for some hours.

One characteristic of gamma rays is their high ability of penetrating medium deeper than the others radiations.

2.3.4 Radioactive decay law

When radioactive substances undergo radioactive decay processes the number of radioactive nuclei inexorably decreases with time. The decay is statistical in nature, meaning that it is impossible to predict exactly when a radioisotope will decay and it is well described through an exponential law.

If the radioactive sample contains N nuclei at time t and if there aren't new nuclei introduced in the sample, the number of decays dN happening in a time interval dt is proportional to N , so

$$\lambda = -\frac{(dN/dt)}{N} \quad (2.3)$$

in which λ is the *decay constant* and is characteristic of each isotope. It represents the probability of decaying in unit time. So this equation explains that this probability is constant whatever the age of the atoms is.

The solution of (2.3) leads to an exponential law called the *radioactive decay law*

$$N(t) = N_0 e^{-\lambda t} \quad (2.4)$$

where N_0 is the original number of radionuclides at $t = 0$.

One of the main features of a radioactive nucleus is its *half-life*, $t_{1/2}$. It indicates the time needed for the decaying nuclei to halve. It can range from a fraction of a second to millions of years. The shorter ones belong to nuclei that decay easily, the longer ones to nuclei which have some obstacles and so are slow in decaying. The value of half-lives can be obtained by imposing $N = N_0/2$ and the result is

$$t_{1/2} = \frac{\ln(2)}{\lambda} \quad (2.5)$$

In addition to the half-life, there is the *mean lifetime*, τ . It is defined as the average time that a nucleus survives before its decay. By definition it is the inverse of decay constant so can be expressed as

$$\tau = \frac{1}{\lambda} \quad (2.6)$$

From equation (2.4) it is possible to determine which is the number of decayed nuclei in any given moment. This is the decay rate and is known as *activity*. Activity can be expressed as

$$A(t) = \lambda N(t) = \lambda N_0 e^{-\lambda t} = A_0 e^{-\lambda t} \quad (2.7)$$

where $A_0 = \lambda N_0$ is the activity at the time $t = 0$. From equation (2.7) is possible to notice that, as the number of radionuclides, also the activity decays exponentially with time.

The SI unit for activity is the becquerel (Bq) that corresponds to one disintegration per second. However, for historical reasons, activity is still widely measured in Curies (Ci), defined as

$$1Ci = 3.7 \times 10^{10} \frac{\text{decays}}{s}$$

where 1 Ci is approximately the amount of radioactivity emitted by 1 g of radium-226.

2.4 Interaction of photons in matter

To reveal the decays occurred in the target it is necessary to detect the photons emitted by the radioactive species. Since photons haven't an electric charge, they can't undergo inelastic collisions typical of charged particles. So gamma rays have their characteristic interactions in matter. Those are:

- photoelectric effect;
- Compton scattering (including Thomson and Rayleigh scattering);
- pair production.

Those processes have relatively small cross sections determining the high penetration of photons in matter compared to charged particles.

2.4.1 Photoelectric effect

In a photoelectric interaction a photon transfers all its energy to an electron in an atomic shell. Generally, the electron involved is one of them with a relatively high binding energy in the inner shells of the atom. As a result, the electron is ejected from the atom. It is obvious that the process can happen only if the photon has sufficient energy to overcome the electron binding energy and, in the case it has, the energy of the outgoing electron is

$$E_{e^-} = h\nu - E_b \quad (2.8)$$

where $h\nu$ is the photon energy and E_b is the electron binding energy.

Subsequently an electron from an outer shell fills the vacancy left by the ejected electron. The difference in energy between the two shells gives birth to a characteristic X-ray, as can be seen in the upper part of figure 2.2. The filling electron leaves a new hole that can be occupied by another atomic electron, so the process can be iterated. Since level energies are different for each element, X-rays can be exploited to identify a material.

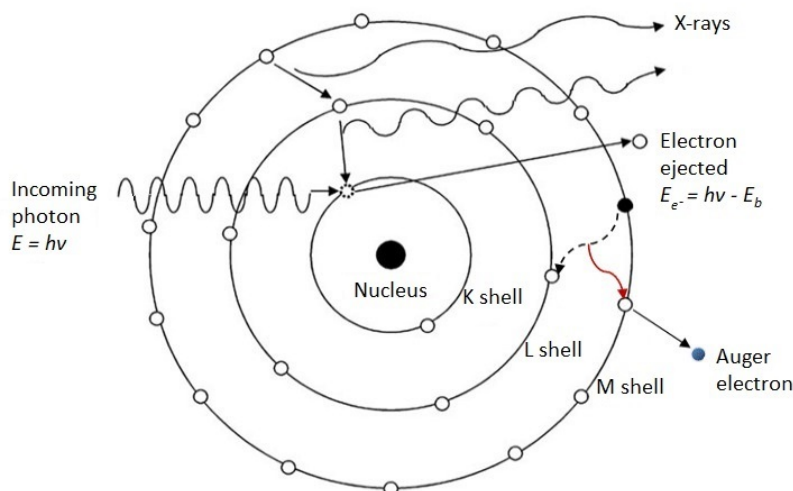


Figure 2.2: Emission of an electron and X-rays due to photoelectric interaction of a photon with an atom (up); emission of an Auger electron as an alternative to X-rays in photoelectric effect (down). K, L and M are the names universally given to the different energy shells.

Sometimes, instead, the energy released can be used to extract an electron from the most external orbits, in the way represented in the bottom part of figure 2.2. This other type of ejected electron is named *Auger electron*.

A typical photoelectric cross section as a function of incident photon energy is in figure 2.3. The L and K edges represented in the figure are the *absorption edges*. When the incoming photon energy approaches the binding energy of the atomic electron in the K or the L shell, the probability for the photoelectric effect to occur increases abruptly because the number of available electrons for the interaction grows.

It is interesting to observe that, for photon energies of the order of MeV, the photoelectric cross section goes as Z to 4th or 5th power. This means that

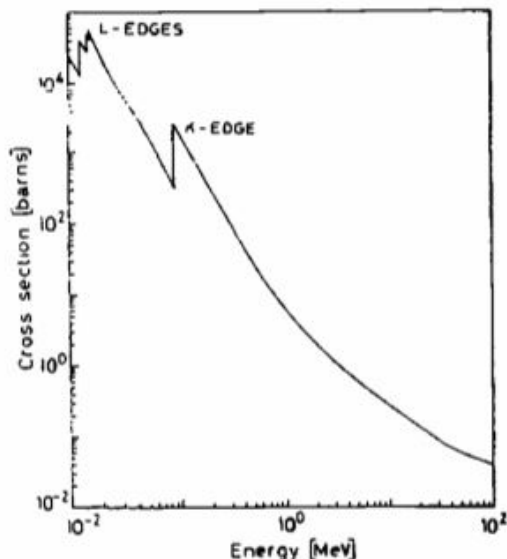


Figure 2.3: Calculated photoelectric cross section for lead [11].

high Z materials are preferable if the photoelectric absorption is desired. This is an aspect to consider when choosing a γ -ray detector. The photoelectric cross section is also proportional to $E^{-3.5}$.

2.4.2 Compton scattering

The Compton scattering is the interaction of the photon with a free electron. Obviously in matter the electrons are bound but, if the photon energy is high enough in comparison with the electrons binding energy, they can be considered as essentially free. This is generally the case of the most external atomic electrons. In a Compton interaction the photon releases only a portion of its energy to an electron; the result is an ejected electron and a scattered photon with decreased energy. The process is represented in figure 2.4. The energy transferred to the electron in a Compton interaction is small when the incoming photon has a low energy while, when the photon energy is very high (10 to 100 MeV), most of the energy goes to the recoil electron, so few interactions are needed to completely absorb the photon energy. This can be seen in the recoil electrons energy spectra in figure 2.5, for different incident photons energies. The Compton edges visible in figure 2.5 correspond to the maximum energy given to the electron and can be calculated as

$$E_{max} = h\nu \frac{\frac{2h\nu}{mc^2}}{1 + \frac{2h\nu}{mc^2}} \quad (2.9)$$

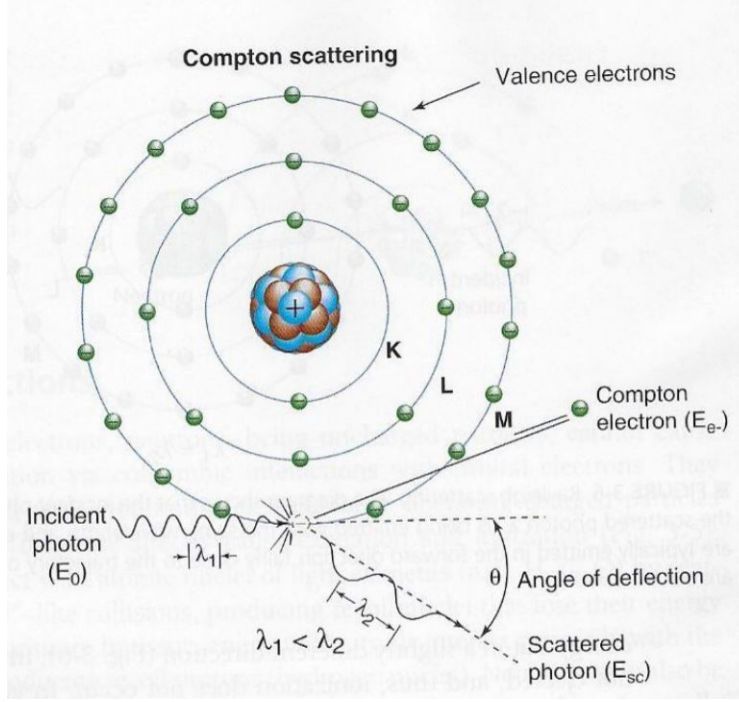


Figure 2.4: Compton scattering process causing the ejection of an outer atomic electron. The scattered photon shows a reduced energy and an increased wavelength [12].

Compton scattering is probably one of the best understood processes among all the photon interactions. Its cross section can be evaluated thanks to the Klein-Nishina formula, which represents the differential cross section

$$\frac{d\sigma}{d\Omega} = \frac{r_e^2}{2} \frac{1}{\left[1 + \frac{h\nu}{mc^2} (1 - \cos\theta)\right]^2} \left(1 + \cos^2\theta + \frac{\left(\frac{h\nu}{mc^2}\right)^2 (1 - \cos\theta)^2}{1 + \frac{h\nu}{mc^2} (1 - \cos\theta)} \right) \quad (2.10)$$

where r_e is the classical electron radius and $m=511$ keV is the electron mass. Integration of this equation over $d\Omega$, where $d\Omega$ is the solid angle element, gives the total cross section σ_C . The total cross section can be subdivided into Compton scattered, σ_s , and Compton absorption, σ_a , cross

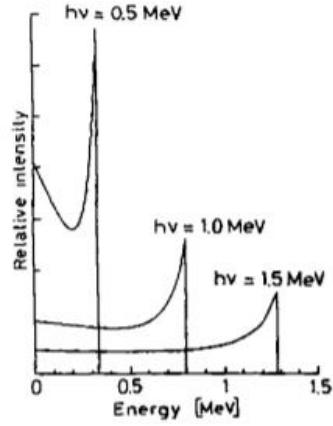


Figure 2.5: Energy distribution of Compton recoil electrons [11]. The most energetic incoming photon ($h\nu=1.5$ MeV) has the maximum amount of possible transferred energy ($E\sim 1.3$ MeV). The sharp drops are known as *Compton edges*.

sections. σ_s defines the average fraction of energy remaining in the scattered photon, while σ_a indicates the average energy transferred to the ejected electron. The relation between them can be observed in figure 2.6, and is described as

$$\sigma_C = \sigma_s + \sigma_a \quad (2.11)$$

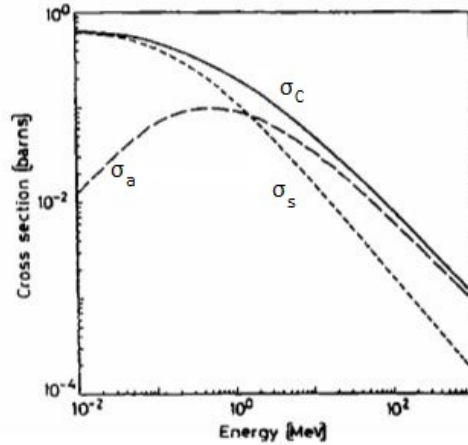


Figure 2.6: Total Compton scattering cross sections [11].

At low energies, in figure 2.6, σ_s is approximately equal to the total cross section; at this photon energies, in fact, the recoil electron receives a negligible

fraction of energy, as it is also deductible from figure 2.5. As energy increases ($h\nu > 2 \text{ MeV}$), the energy transmitted to the electron becomes larger than that available for the scattered photon.

The Compton total cross section itself does not depend on Z , but all the Z electrons of the atom should be taken into account so the final cross section, which includes the multiplication for Z , shows a linear dependence on Z .

Rayleigh and Thomson scattering are classical processes which don't include any deposition of energy in the medium. All the incident photon energy is scattered and the wavelength remains the same. The only variation is in the direction. Those types of interaction are possible only at low photon energies.

2.4.3 Pair production

In pair production a photon, interacting with the nucleus strong electric field, converts into an electron-positron pair. An essential condition to make the pair production possible, is the minimum photon energy of 1.022 MeV , which represents two times the electron (or positron) mass. The presence of a third body, the nucleus, is necessary for momentum and energy conservation.

Sometimes the interaction happens with the electric field of an orbital electron, generating a triplet production. In this case the photon energy value should be at least 2.044 MeV .

The pair or triplet production cross section shows a dependence on Z^2 .

Both the processes are illustrated in figure 2.7.

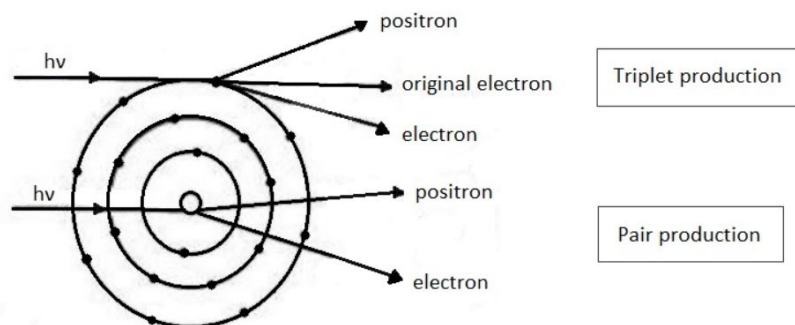


Figure 2.7: Absorption of a photon by triplet (up) and pair (down) productions.

2.4.4 Photons total cross section

The total probability for a photon crossing the medium to interact is the sum of the single cross sections for the previous single processes

$$\sigma_{tot} = \sigma_{p.e.} + Z\sigma_C + \sigma_{pair} \quad (2.12)$$

An example of the trend of this equation, that strongly depend on the material considered, is in figure 2.8.

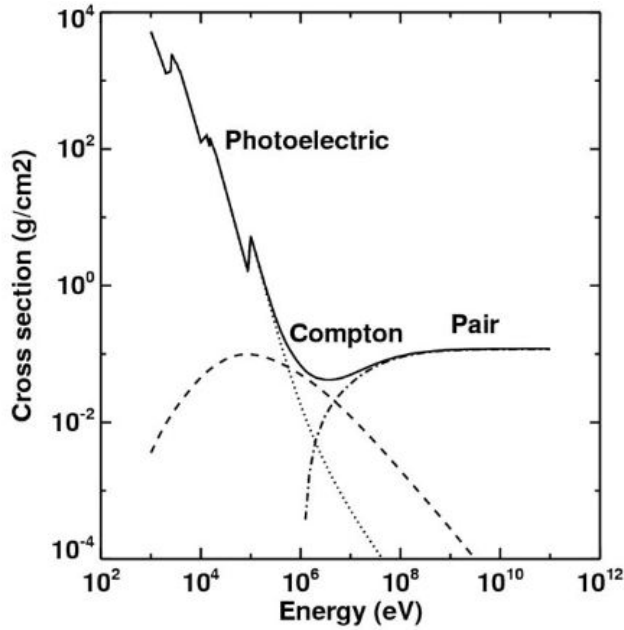


Figure 2.8: Total photon absorption cross section for lead. The solid line is the total cross section. The dashed line is Compton scattering contribution, the dotted line is due to the photoelectric effect and the dash-dot line represents the pair production.

It is clear that at low energies the photoelectric effect is the predominant one. Then, as the energy increases, first the Compton effect becomes important and subsequently the pair production, at energies of some MeV. The importance of the three different interactions is related to the material crossed by the photon as can be seen in figure 2.9.

The Compton scattering is more influent in low Z materials while pair production and photoelectric effect predominate in high Z materials, at high and low energies respectively, as can be observed in the two plots in figure 2.9. This behavior is confirmed also in figure 2.10. Here elements with low

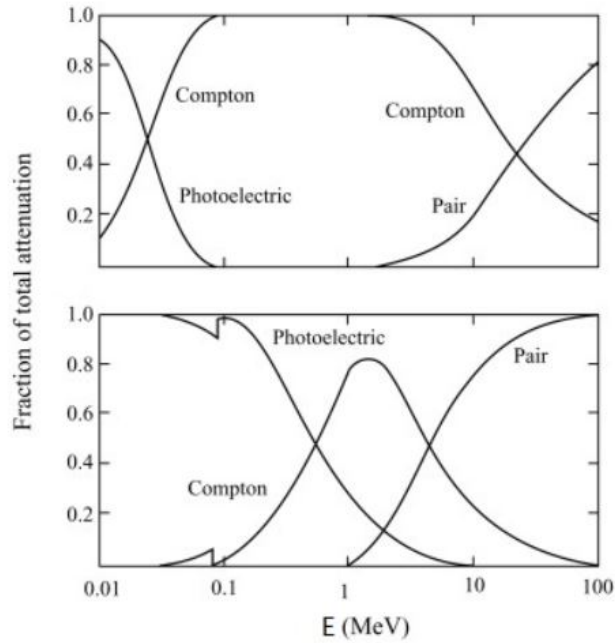


Figure 2.9: Relative probability of different photon effects at different energies in carbon (up) and lead (down). Carbon represents a low Z material while lead is a high Z one.

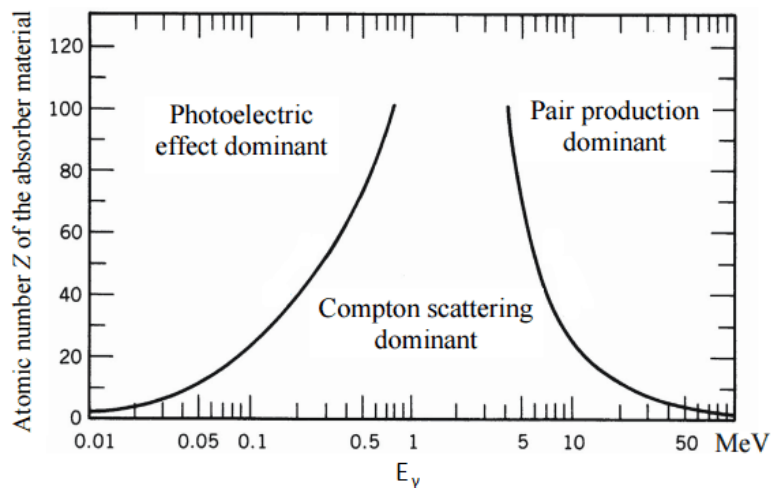


Figure 2.10: The three γ -ray interaction processes and their domination regions for different Z of the medium and at different energies.

Z cause mainly Compton scattering, which, instead, is less probable in high Z materials.

Those are the ways in which photons interact also in the detector volume, generating γ -ray spectra. The presence of charged particles among the results of all the processes allows the detection of photons produced by radioactive nuclei decays.

2.5 Typical features of γ -spectra

A photon spectrum usually consists of discrete lines of very small width and a continuous distribution due to the different possible photon interactions described just before. The lines are nothing more than total absorption peaks and provide the useful information. The rest can be considered as spectral background, unwanted but unavoidable. The spectrum for a single radioactive nucleus is shown in figure 2.11 with all its main features.

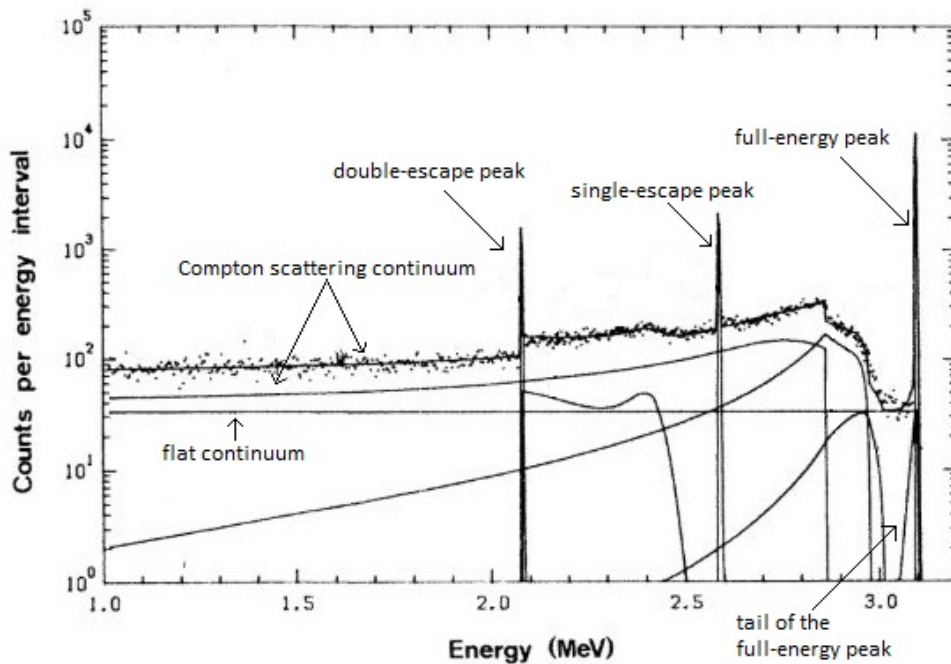


Figure 2.11: Experimental pulse-height spectrum with its components [13].

In the photoelectric effect an electron is released with kinetic energy equal to the energy of the incident photon minus the binding energy (equation 2.8). The binding energy should be found later in form of characteristic X-rays

originating from the rearrangement of the atomic electrons, after the emission of the photoelectron. In turn X-rays can interact, through a photoelectric effect, with less bound atomic electrons. In the end the sum of the kinetic energies of the created electrons must equal the original γ -ray energy. This is true only if three conditions are fulfilled:

- X-rays produced have to be absorbed in the detector. If they escape, they contribute to the formation of the X-ray escape peaks at lower energies compared to the total absorption peak.
- Photoelectrons must lose their entire energy in the detector sensitive volume. Escaping, photoelectrons generate the continuum from zero to full energy.
- Trapping effects and charge collecting losses (described in the following chapter) have to be negligible. If they are not negligible, the effect is a tailing of the peak on the low-energy side.

The photoelectric absorption, ideal for gamma ray energy measurements, dominates at low energies. In the energy range from 150 keV to 9 MeV for germanium, and from 50 keV to 15 MeV for silicon [13], the most frequent process is the Compton scattering. The two extreme situations that may occur are:

- The scattering angle is $\theta \cong 0$. In this case the recoil Compton electron gains a little amount of energy while the scattered gamma-ray has nearly the same energy of the incoming photon.
- The scattering angle is $\theta = \pi$. If this is the case, the incident gamma-ray is backscattered towards its direction of origin and the recoil electron continues along the direction of incidence. This is the way in which there is the maximum energy transfer to an electron in a single Compton scattering.

In general, between those two extremes, all the scattering angles are possible. So assuming that only Compton electrons energy is absorbed in the detector, they give rise to a continuous distribution extending from zero up to the maximum energy transferable. The sharp theoretical Compton edge in the continuum distribution, visible in figure 2.5, is smeared out in the spectrum in figure 2.11. The effect is a number of counts lower than expected and a maximum energy slightly lower. The cause is the binding energy of detector material electrons, while the theoretical assumption for the Compton interaction is that electrons are initially free.

But the Compton scattering has, in the final state, also the scattered photon which can interact again in the detector. If it undergoes the photoelectric effect, then the sum of the Compton electron and the photoelectron contributes to the full-energy peak. On the contrary, if it interacts by a further Compton scattering and the second scattered photon escapes from the detector crystal, the pulse appears again anywhere in the continuum below the peak.

It should be reminded that the pair production is possible only if the photon has an energy at least equal to $2m_0c^2=1.022$ MeV. Actually, this process becomes important only at photon energies above 1.5 MeV. After pair production, the positron created quickly annihilates with an electron in the detector volume, emitting two annihilation photons. If both the quanta escape, the absorption of the kinetic energy of the electron-positron pair results in a double-escape peak at an energy of $E-2m_0c^2$, where E is the initial photon energy. If one of the annihilation photon interacts in the detector, instead, in the spectrum appears a single-escape peak at $E-m_0c^2$. Moreover, if both the generated quanta remain in the detector, the result is in the full-energy peak.

The photons emitted from the source can also interact with the surrounding shielding material rather than with the detector. Figure 2.12 shows how the resulting secondary photons, namely X-rays, Compton scattered and annihilation quanta, may reach the detector and contribute to the spectrum.

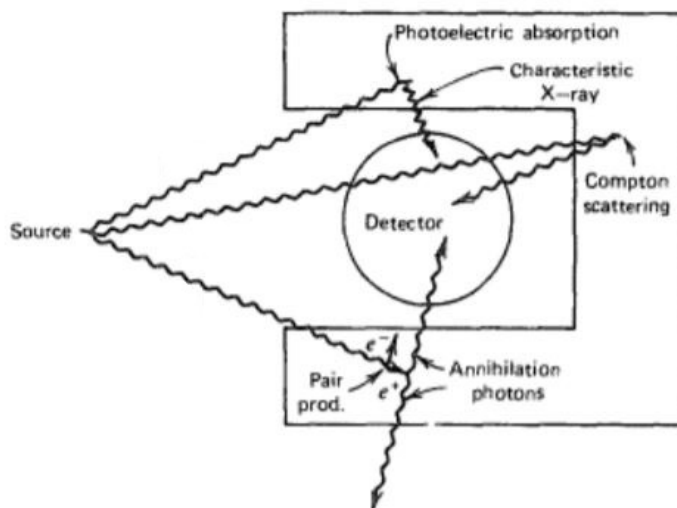


Figure 2.12: Example of how the three different photon interactions can occur in shielding material around the detector.

The photoelectric absorption is responsible of the emission of characteristic X-rays when the electrons in the atom are rearranged. If those X-rays reach the detector and interact, the corresponding peaks may be observed in the spectrum.

The photons scattered, coming from the Compton interaction with the surrounding material, can have scattering angles in the range from 0 to π . More frequently the photons are backscattered and this causes the formation of the backscatter peak, obviously at low energies considering that for $\theta = \pi$ almost all the photon energy is given to the electron in the surrounding material involved in the Compton process.

The pair production, for photons of high energy, with the shielding material gives rise to electron-positron pairs. The following positrons annihilation create photons that, reaching the detector, generate the peak at 511 keV. Contribution to this peak may also originate from annihilation of positrons emitted in β^+ decay of the radionuclide under study.

All this extra peaks can be seen in figure 2.13.

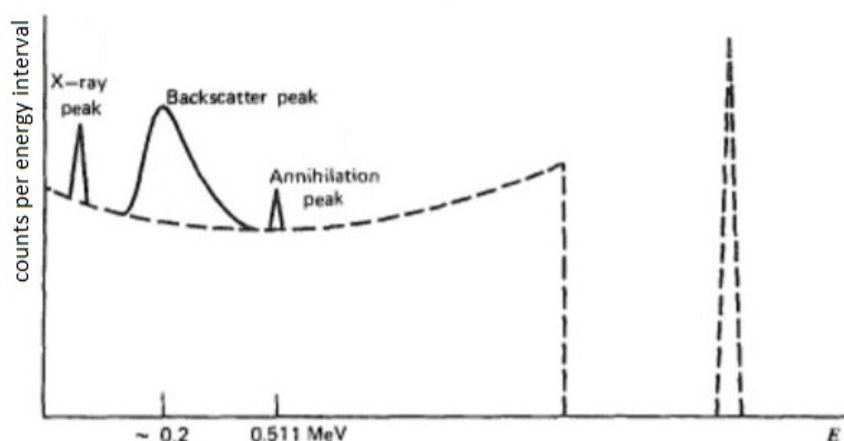


Figure 2.13: Effects of the surrounding material on detector response. The dashed line is the theoretical expected spectrum while the solid line gives the effects of material around the detector.

In γ -ray spectrometry, all the elements described, constituting the spectrum, except for the full-energy peak, are in addition to the background, generally formed by the environmental radiation. The full energy-peak, instead, represents the signal.

When the source contain more than one radionuclide, all the components for each radionuclide appear together in the same spectrum. This is the case of the spectra analyzed in this thesis. One of the spectra acquired for the measurements of the cross sections of ^{47}Sc and its contaminants is reported

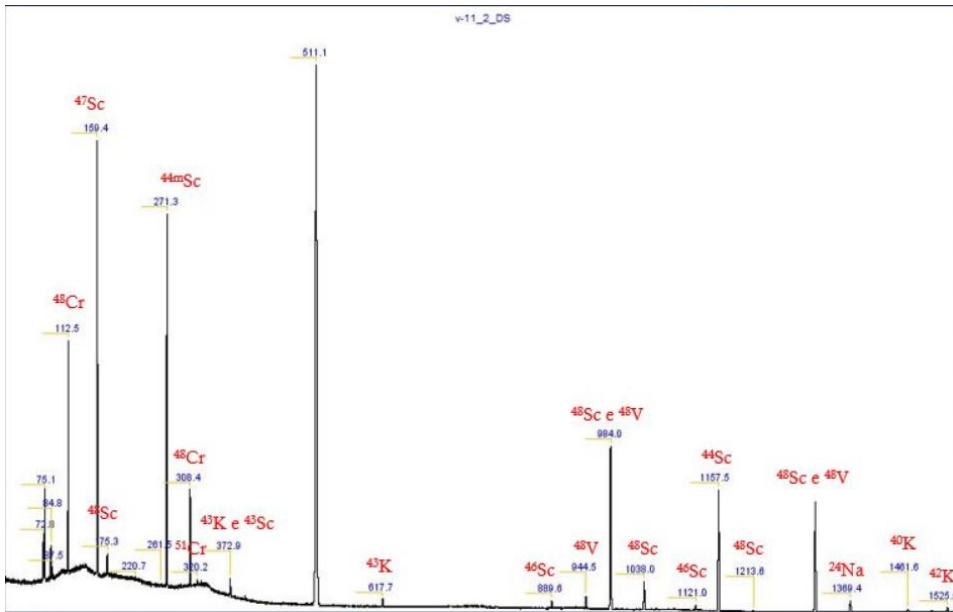


Figure 2.14: Spectrum acquired during the first irradiation run at AR-RONAX. Energies of gamma-rays detected and emitter radionuclides are reported.

in figure 2.14. Among the previous listed features, the most visible is surely the annihilation peak at 511 keV together with all the full-energy peaks.

The gamma-peaks in figure 2.14 have a Gaussian shape. Ideally one peak should have a single energy value corresponding to the incoming photon energy. The Gaussian distribution around this energy value is a consequence of stochastic effects of the collection processes in the detector and conversion processes.

Spectrum in figure 2.14 and others similar are analyzed to obtain cross sections values, according to the procedure described in chapter 4.

Chapter 3

Instruments for cross sections measurements

The procedure needed to measure isotopes cross sections requires the use of different devices. First of all an accelerator generates the particle beam, whose energy spread has to be as low as possible and the intensity should be suitable for the foils activation, maintaining the total activity as low as possible. The nuclear reactions of interest occur in the target, specifically assembled for the purpose and composed by thin metal foils. After the bombardment, the target is disassembled and each irradiated sample is collected to perform gamma-spectrometry acquisitions. In particular, gamma-ray spectrometry measurements were performed with a dedicated HPGe detector. From the measured spectra is possible to calculate the nuclear cross sections of interest, as described in the following chapter. In this chapter the different instruments needed for a cross section measurements are described.

3.1 Cyclotron accelerators

The primitive idea of the cyclotron was elaborated by Ernest Lawrence at the University of California at Berkeley in 1929 [14]. A cyclotron is basically a circular device in which a particle beam repeats up to hundreds time the same cycle. At each time the beam undergoes an energy increase till reaching the MeV energy range. This is possible thanks to the electromagnets and the cavities. Two cylindrical electromagnets generate a magnetic field between them, perpendicular to their circular surfaces. The magnetic field created is responsible for the bending of the particles path which results of circular form. In the center, between the two electromagnets, immersed in the magnetic field, there are two semi-circular cavities. They are separated by two opposite

gaps where an alternate voltage source is applied. With this configuration, when the particles are injected in the middle of the cyclotron, they don't feel any electric field but only the magnetic field that causes a circular track. Particles undergo an acceleration and gain a small energy amount each time they cross the gap. This acceleration is possible at each turn, by applying the alternate voltage with a half-period equal to the particles semicircular orbital time. The energy gain means a larger radius of the path and a higher speed since the time to complete a cycle remains constant. The final result is a spiral motion outwards. The schematic representation is in figure ??.

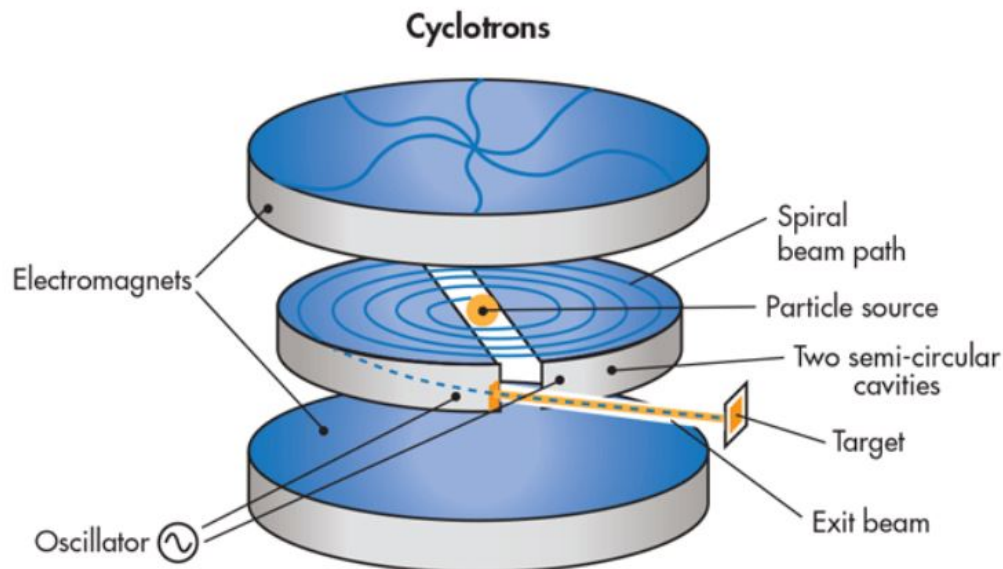


Figure 3.1: Simplified diagram of a cyclotron. The beam is pushed outwards starting from the center, until it is extracted and directed against a target.

The Lorentz force in the circular orbit provides the centripetal acceleration to maintain the circular motion, so

$$F = qvB = \frac{mv^2}{r} \tag{3.1}$$

from which the time necessary for a semicircular orbit is

$$t = \frac{\pi r}{v} = \frac{m\pi}{qB} \quad (3.2)$$

The frequency of the alternate voltage is

$$\nu = \frac{1}{2t} = \frac{qB}{2m\pi} \quad (3.3)$$

which is often called the *cyclotron frequency*. Equation 3.3 is important because shows that ν and B are linked: for a given magnetic field strength, the frequency can only have a certain value at which the resonance is achieved.

As mentioned before, when the particles spiral outwards they get quicker. The maximum velocity is reached at the largest possible radius R and, according to equation 3.1, it is

$$v_{max} = \frac{qBR}{m} \quad (3.4)$$

leading to a maximum kinetic energy equals to

$$T = \frac{1}{2}mv_{max}^2 = \frac{q^2B^2R^2}{2m} \quad (3.5)$$

Looking at equation 3.5 it seems that cyclotrons with large magnetic fields and large radii are advantageous. Moreover, the voltage amplitude appear irrelevant. A larger voltage implies a larger gain of energy at each orbit traveled, but in the end the particles don't reach a higher energy, simply they leave the cyclotron before, after completing a smaller number of cycles.

A limit on the cyclotron size is put surely by the economical aspect but there is also a physical reason. The relativistic behavior of accelerated particles implies that to maintain the resonance condition, as the velocity increases, the magnetic field must be also increased. So at larger radii must correspond larger magnetic fields. However, in the cyclotrons magnetic fields are constant and fixed, so there is no acceptable way to compensate for the relativistic effect. This imposes a limit on the size of such machines.

3.2 LNL future cyclotron and facility

At INFN-LNL (Laboratori Nazionali di Legnaro) the LARAMED project started in 2012, funded by Italian Ministry of University and Research (MIUR) with a Premium project preseted by INFN. LARAMED is born in the SPES (Selective Production of Exotic Species) frame, the future of the laboratory [3]. The topics treated in the four phases of SPES, named with the letters of

the Greek alphabet, are: alpha, the installation of the cyclotron itself and the experimental infrastructures around it; beta, the acceleration of neutron-rich unstable nuclei as the ones generated in the first stellar stages; gamma, the production of radioisotopes of medical interest; delta, the development of a neutron source for multidisciplinary applications.

At the heart of SPES facility there is the model BCSI 70p cyclotron, manufactured by BestTM Cyclotron System Inc. (Vancouver, BC, Canada) and installed in the central bunker of the SPES building. The cyclotron is reported in figure 3.2.



Figure 3.2: The high-energy (70MeV) and high-current ($750\mu\text{A}$ proton beam cyclotron installed at INFN-LNL.

The layout of the SPES bunkers (with the cyclotron shown in the mail vault) and the surrounding experimental areas are reported in figure 3.3. As can be seen in figure 3.3, the cyclotron is able to provide two outgoing beams of accelerated protons, with a tunable energy in the range from 35 MeV to 70 MeV and a maximum current of $750\mu\text{A}$. Each of the two beam lines is further split, through two consecutive switching magnets, into additional sub-lines directed towards different research bunkers. Among those beam lines, two are assigned to LARAMED research activities in the RILAB (RadioIsotopes LABORatories) facility and other two arrive to the RIFAC (RadioIsotopes FACTory) section. The RIFAC space is implemented for the radioisotopes massive production with the aim of hospital and clinical departments distribution for routine and clinical research employments.

In summary LARAMED has four bunkers named RI#1, RI#2, RI#3 and A9c (figure 3.3, where a proton current of $500\mu\text{A}$ (RI#1, RI#2), $300\mu\text{A}$

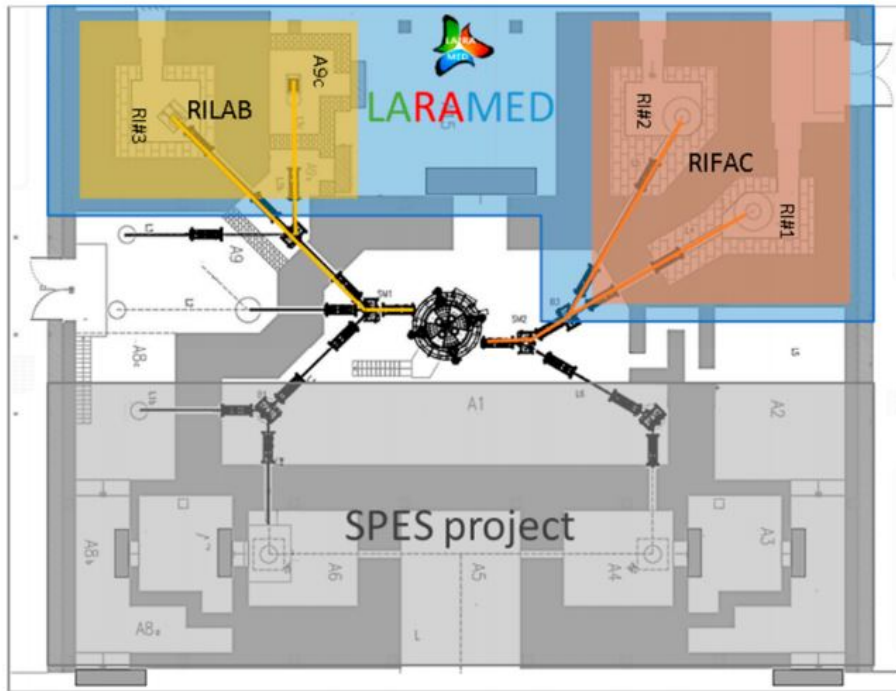


Figure 3.3: Layout of the SPES building (-1 level); the cyclotron is also represented with all beamlines [2].

(RI#3) and 100 nA (A9c) will be available. The beam energies can be set in the range between 35 MeV and 70 MeV as mentioned before.

There are very few high-energy and high-intensity cyclotrons around the world with similar characteristics: the ARRONAX facility in France, mainly devoted to routine radioisotopes supply and partially used for research activities, and ZEVACOR in USA, designed for radioisotopes production only. This clarifies immediately how important could be the LARAMED project in the global scenario of medical radionuclides production.

The LARAMED beam lines just described are under construction right now. In the meanwhile, different research topics concerning conventional and emerging medical radionuclides are approached exploiting the ARRONAX cyclotron. This is the case of the study of ^{47}Sc and contaminants production, the aim of the PASTA project.

3.3 The ARRONAX cyclotron

The ARRONAX facility disposes of a high-energy and high-intensity IBA cyclotron (Cyclone 70), installed at Nantes (France) in 2007 and fully operational since January 2011 [15]. This facility is funded by the Regional Council of Pays de la Loire, the University of Nantes, the French government (with the Centre National de la Recherche Scientifique, CNRS, and the Institut National de la Sante et de la Recherche Medicale, INSERM) and the European Union. The aim for ARRONAX high-energy and high-intensity cyclotron is the production of radionuclides for systematic diagnostic and therapeutic applications. This cyclotron is able to accelerate both positive and negative ions up to 70 MeV. All the available beams at ARRONAX and their characteristics are reported in table 3.1.

Table 3.1: Characteristics of the available beams at ARRONAX [4].

Beam	Accelerated particles	Energy range (MeV)	Intensity (μA)
Protons	H^-	30-70	<350
Protons	HH^+	17.5	<50
Deuterons	D^-	15-35	<50
α particles	He^{++}	70	<35

Positive ions are extracted with an electromagnetic septum which allows only fixed energy for proton or α particle beams. Negative ions are extracted using the stripper foil technique. This method delivers a large incident energy range for particle beams. For proton beams this range goes from 30 MeV up to 70 MeV. This is the technique used to generate the proton beam used in cross sections measurements of the PASTA project.

At the ARRONAX facility six experimental vaults are available, named AX, A1, A2, P1, P2 and P3, and depicted in figure 3.4. Due to different extraction methods protons and deuterons are available in all the vaults while α particles can be used only in vaults A1, A2 and AX.

Vaults A1, A2, P2 and P3 are devoted to radionuclides production and are supplied with pneumatic transfer system which connects to hot cells. P1 is employed for the development of a neutron activator system (collaboration AAA company). The last vault AX is constructed for radiolysis, radiobiology and physics experiments.

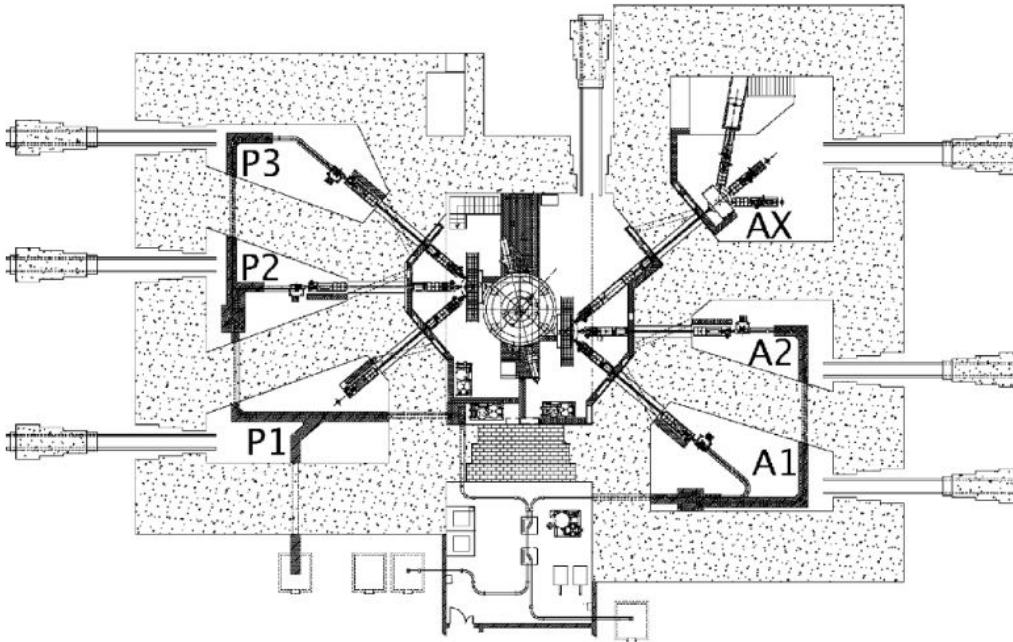


Figure 3.4: Schematic view of the ARRONAX facility. The different laboratories located around the vaults are not shown [4].

The existence of high-energy and high-intensity cyclotron, like ARRONAX and SPES ones, are necessary to realize future clinical progresses in nuclear medicine.

3.4 Stacked-foils target assembling

The realization of the suitable target, able to guarantee an easy handling and to allow the measurement of several cross section values at different proton energies, during the same bombardment, is an important aspect of the entire process.

The stacked-foils technique was already used in the past and consists in piling different layers of different materials properly chosen depending on reactions needed. Some of those foils are target foils while the others are monitor or degradator foils; all of them are appropriately alternated to constitute the final target structure. To avoid the presence of air between foils and to keep the alignment, a dedicated target holder is used. This support also introduces a limit on the maximum thickness of the whole target as a

consequence of its capacity. The stacked-foils technique allows to bombard more than one target foil in each irradiation run, where the proton beam incident energy varies from one target foil to the other. To accomplish this task, the energy degrader foils are used, usually composed by ^{nat}Al material. Those layers cause the energy loss of the protons constituting the beam before reaching a new target layer. The monitor foils, instead, are added to extrapolate the monitor reactions necessary to calculate the proton beam flux along the stacked-target.

Among all the proton-induced reactions producing ^{47}Sc , the most promising are $^{50}\text{Ti}(p,\alpha)$, $^{49}\text{Ti}(p,2pn)$, $^{48}\text{Ti}(p,2p)$ and $^{nat}\text{V}(p,x)$. The quicker and cheaper to use is the natural Vanadium. It is suitable with its natural abundance (99.750% ^{51}V and 0.250% ^{50}V), so it doesn't require any enrichment process, and it is economic for this reason.

In the first three irradiation runs performed at ARRONAX were used only ^{nat}V target foils together with Aluminium as monitor and degrader layers. In the last three, instead, were inserted the ^{48}Ti deposited target foils, in addition to the ^{nat}V ones, and as monitor foils was used Nickel. The deposition of ^{48}Ti is made on an Aluminium support (25 μm thick). The degraders used are always 0.5-1.0 mm thick aluminium foils. Table 3.2 summarize the number of target foils in each irradiation run. Anyway in this thesis work the attention is focused on the ^{47}Sc production from ^{nat}V targets so the knowledge of ^{48}Ti is necessary only in the energy calculation described in the next chapter.

Table 3.2: Features of targets used at ARRONAX during the irradiation runs performed.

Run #	Date	Target material	Target foils #	E_P (MeV)	Duration (min)
1	11-4-2017	^{nat}V	3	70.3	90
2	27-6-2017	^{nat}V	3	54.0	90
3	4-7-2017	^{nat}V	3	61.0	90
4	10-10-2017	^{48}Ti	3	34.0	90
		^{nat}V	3		
5	22-11-2017	^{48}Ti	4	40.0	50
		^{nat}V	1		
6	17-4-2018	^{48}Ti	3	34.0	90
		^{nat}V	1		

Representations of targets with and without ^{48}Ti foils are in figure 3.5 and 3.6.



Figure 3.5: Target used in the first irradiation run. a similar structure was used also in the second and third irradiation runs.

The numbers reported near the element symbols are codes arbitrary established in order to distinguish the different foils during data analysis. The target and monitor foils are occasionally inverted between them to take into account the recoil effect of reactions occurring in both the layers. When the accelerated beam crosses the stacked-foils target, it can cause the passage of some produced radionuclides from the layer where their production took place to the following one. As a consequence, the subsequent foil shows unexpected peaks in the spectra, corresponding to the radioisotopes generated in the previous layer. This is called recoil effect. So the stacked-foil technique can be exploited to know how many radionuclides of each species are pulled in the following layer.

The Aluminium layer at the end of the target is used as support to give more rigidity and strength to the whole target.

The Aluminium foils paired with Titanium ones, shown in the of figure 3.6, are the supports over which the Titanium powder is deposited. They



Figure 3.6: Target used in the fourth irradiation run. Targets with similar elements but with a different disposition are used in fifth and sixth runs.

together constitute a single foil, as can be seen the photograph reported in figure 3.7, but are considered independently when calculating the proton energy in each foil of the stacked target.



Figure 3.7: Photograph of the stacked foil target used in the fourth irradiation run. The second layer named $^{48}\text{Ti}+^{\text{nat}}\text{Al}$ includes all the foils indicated as Al-42, Ti-42, Ti-43 and Ti-43 in figure 3.6.

All the layers reported in figure 3.7 are inserted, stacked, in the target holder shown in figure 3.8. The total thickness of all the foils should not exceed 3 mm in total because this target holder, used during operations at ARRONAX, imposes 3 mm as target thickness limit.

After the irradiation of the target, to measure samples cross sections, is used γ -spectrometry. This requires a HPGe semiconductor detector.

3.5 Semiconductor detectors

In the second chapter were presented the different ways in which gamma radiation transfers energy to electrons, and in case of pair production also to positrons, interacting with matter. These particles lose their kinetic energy by scattering around within the detector, creating ion-electron pairs. This secondary population forms the basis of the detector signal. In particular, the collection of electron-hole pairs created generates the electrical signal, proportional to the number of pairs and thus to kinetic energy deposited in the detector. The most obvious way to collect the electron-hole pairs is to supply an electric field. This solution requires that the detector has suitable electrical characteristics. Semiconductor detectors satisfy this request thanks to their band structure.

In a free atom the electrons are disposed in precisely determined energy levels. Combining some atoms together into a solid structure broadens those energy levels into energy bands, each of which can contain a fixed number of electrons. The uppermost occupied of those bands is the valence band, responsible of the chemical reactions. In this band the electrons are tightly bound and associated to their respective atoms. Electrons are allowed to



Figure 3.8: Opened (up left) and assembled (up right) target-holder, collimator and support (down left) and alignment procedure on the beam line at the ARRONAX facility (down right).

freely migrate across the entire crystal, if they are able to move to the empty conduction band. In this energy band electrons can go from an atom to another. Between the energy bands there are regions forbidden for electrons, called gap band, as shown in figure 3.9, for a conductor, a semiconductor and an insulator. If electrons can reach the valence band, then, applying an electric external field, a current is created through the material.

In an insulator an electron should gain an energy equal to 10 eV to cross the band gap and jump from the valence band to the conduction one. The thermal excitation can not fulfill this energy amount so insulators can not be crossed by a current. In a metal, which is a conductive material, the conduction band is continuous with the valence band so the conduction band is always populated. Even a small external electric field will induce a current to flow. The semiconductors structure is similar to insulator's one but the band gap is smaller, of the order of 1 eV, an energy achievable through thermal excitation. Under normal conditions there is always a small electron population in the conduction band. However, if the semiconductor is cooled, all the electrons fall into the valence band and the conductivity of the semiconductor is reduced. This also means that the background current is reduced and that the excitation due to low energy deposition of the interacting gamma rays is easier to detect.

On the other hand, when an electron leaves the valence band to arrive in the conduction band, in its original position remains a hole. A hole can be

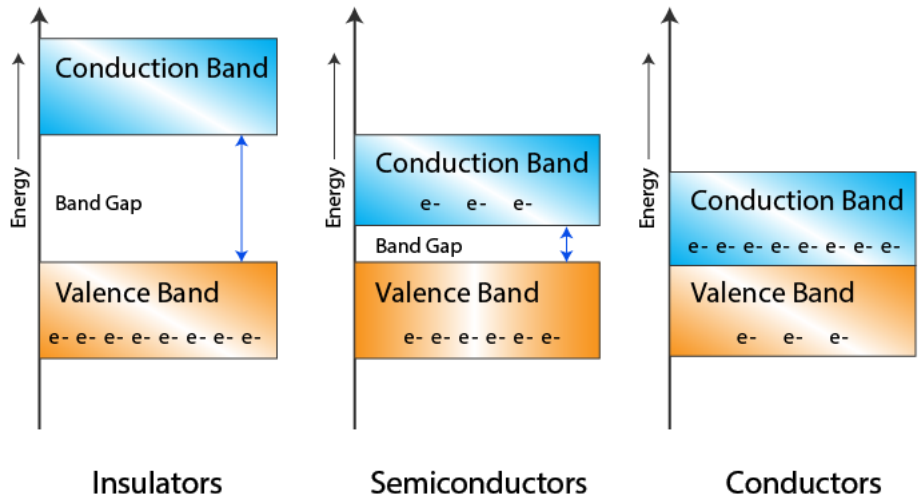


Figure 3.9: Electronic band structures in solids, respectively insulators, semi-conductors and metals.

considered as a positive charge. Another electron from the valence band can fill the vacancy, leaving, in turn, a new hole, and so on. In this way it appears that also the holes move, but towards the opposite direction compared to electrons in the conduction band. In conclusion both the electrons and the holes, called charge carriers, contribute to the detected electric current.

Sometimes it happens that an electron recombines with a hole by dropping from the conduction band into an open level in the valence band, followed by the emission of a photon [11]. This is the *recombination* effect, the reverse of electron-hole generation. This mechanism requires the support of the recombination centers, which are given by the crystal impurities. Those elements add new energy levels in the middle of the band gap. Here an electron can be captured from the conduction band. If during the holding time a hole is also captured the recombination occurs, otherwise the electron is released back to the conduction band. In the recombination centers arises also the *trapping* effect. Trapping is a consequence of the capability of some impurities to capture only one type of charge carriers, so or electrons or holes but not both. After a certain characteristic time, the captured carriers are simply released.

For radiation detection purpose, the existence of impurities causes a reduction of the mean time that charge carriers spend free in the lattice. If this time is shorter than the collection time, the effect is moderate, otherwise

there is a charge lost and incomplete charge collection with a consequent resolution deterioration. Semiconductor detectors therefore require relatively pure crystals.

Known as a semiconductor works, it is clear that when a γ -ray interacts in the semiconductor volume it generates a population of electrons (and positrons). The particles produced have energies greater than thermal energies, so they are able to move electrons of the crystal atoms from the bound energy levels to the conduction band, interacting and giving them their energy. During this process further excitation can occur, giving a cascade of electron-hole pairs for each primary electron. If an electric field is applied, electrons and holes are collected and, in this way, a signal is obtained. The response of a semiconductor should be perfectly linear so, if E is the energy of the incoming radiation and w is the average energy needed to create an electron-hole pair, the number N of pairs produced is

$$N = \frac{E}{w} \quad (3.6)$$

If n is the collection efficiency, then the charge Q collected at the electrodes is

$$Q = n \frac{E}{w} \quad (3.7)$$

and the voltage observed is

$$V = \frac{Q}{C} = n \frac{E}{wC} \quad (3.8)$$

where C is the capacitance. Equation 3.8 shows that the voltage depends linearly on the radiation energy. If the radiation energy is not totally deposited in the sensitive volume, the linearity of the response is lost.

Together with an output proportional to energy, the others characteristics that distinguish an ideal semiconductor are [16]:

- a large absorption coefficient, i.e. a high atomic number Z ;
- good electron and hole mobility;
- high number of electron-hole pairs produced per unit energy, i.e. low w ;
- availability in high purity;
- availability at reasonable cost.

A good candidate satisfying the previous requests is Silicon. It is readily available at reasonable cost but it has low atomic number ($Z=14$), so it is suitable only for low energy photons measurement. A higher atomic number is found in Germanium ($Z=32$); here the photoelectric cross section is about 60 times greater than for Si. However Germanium needs low working temperatures because of its smaller band gap, but its efficiency is so high that Germanium represents the best choice to detect high energy photons, so gamma rays.

An upgrade in the semiconductor technology led to the fabrication of very high purity Germanium, where the purity concentration is less than 10^{10} atoms/cm³. This gave birth to the High Purity Germanium detectors (HPGe), which don't have to be kept at low temperatures all the time, but cooling becomes necessary only when the external voltage is applied. As for previous Germanium detectors, HPGe are mainly used for gamma ray spectroscopy, and they offer the highest resolution available for gamma energies from few keV to 10 MeV.

3.6 The HPGe detector at ARRONAX facility

At ARRONAX, for γ -ray spectrometry, is used a HPGe detector named *Research*, presented in figure 3.10.



Figure 3.10: Research detector used at ARRONAX to acquire γ -spectra.

As all the HPGe detectors, it requires a calibration to elaborate a cor-

rect gamma spectrum. The calibration consists in two steps. First, the correspondence between channels and energies should be found. This is the energy calibration and is independent from the detector geometry. Then it should be extrapolated the relation between the sample activity and the number of count of the corresponding gamma-peak. This one is the efficiency calibration and depends on the geometry chosen. For ^{47}Sc and its contaminants cross section measurements the *Research* detector calibration is made for solid state samples at a distance of 19 cm from the detector. To reach such a distance, a thin plastic support is used. This is the distance also used during measurements. The function used for efficiency calibration is

$$\epsilon(E) = \exp\left(c_1 \cdot E + c_2 + \frac{c_3}{E} + \frac{c_4}{E^2} + \frac{c_5}{E^3} + \frac{c_6}{E^4}\right) \quad (3.9)$$

where the energies E are expressed in MeV and c_{1-6} are parameters determined by applying a fitting curve to some measured efficiency values, relative to specific energies, obtained by using reference solid sources. The values calculated by the fitting procedure are reported in table 3.3. The efficiency results given by equation 3.9 are then employed during the following data analysis phase. The equation is implemented in the *jRadView* program, so that the measured efficiency curve is included in the results window of the program shown in the next chapter.

Table 3.3: Values assumed by parameters in equation 3.9. Those values are referred to energies expressed in MeV.

Coefficient	Value
c_1	-0.17327
c_2	-8.58062
c_3	1.24848
c_4	-0.319716
c_5	0.0446384
c_6	-0.00238326

For precise spectrum measurements it is important to shield the detector with lead to minimize the background in order to improve the signal-to-noise ratio.

Research is used to detect γ -rays emitted by radionuclides produced in the target. At the end of the measurement process different γ -spectra are available and ready to be analyzed.

Chapter 4

Determination of the cross sections to produce radionuclides of medical interest

After the irradiation run and the spectra acquisition procedure, the analysis has to be performed to extrapolate numerical cross section values. Considering the medical application of ^{47}Sc described in previous chapters, particular attention has to be also given to the co-production of all possible contaminants, especially to the other Sc-isotopes, since they cannot be chemically separated from ^{47}Sc . Therefore, the experiments performed during the PASTA project were planned to measure not only the ^{47}Sc cross section, but also the excitation functions of all scandium isotopes (^{48}Sc , ^{46}Sc , ^{44}Sc , ^{44m}Sc , ^{43}Sc) and the additional contaminants (^{51}Cr , ^{49}Cr , ^{48}Cr , ^{48}V , ^{43}K , ^{42}K) co-produced during the ^{nat}V bombardment.

The analysis starts from the spectra, which are all similar to that reported in figure 2.14. In those spectra, peaks corresponding to the ^{47}Sc and the contaminants γ emissions should be identified. This is possible thanks to the National Nuclear Data Center [17], where are available known nuclear data regarding all the nuclides, from the smallest H-isotopes to the most massive Ts-isotopes. The nuclear data exploited in this work, to identify the radioisotopes produced, concerns the γ -emissions and are reported in table 4.1. In the last two rows of table 4.1 are listed the nuclear data of the radionuclides used as monitor; monitor reactions take place in monitor foils of the stacked-foils target described in the previous chapter. Also the monitor reactions should be taken into consideration since it is not possible to have a measure of the proton flux in the different layers of the target during the irradiation run.

Table 4.1: Radionuclides parameters extracted from the NuDat database [17]. The numbers reported in the γ -line and intensity columns near the values are the errors that should be associated.

Isotope	γ -line (keV)	Intensity (%)	$T_{1/2}$ (s)	$dT_{1/2}$ (s)
^{43}Sc	372.9 3	22.5	14007.6	43.2
^{44m}Sc	271.241 10	86.7 3	210966	360
^{44g}Sc	1157.020 15	99.9 4	14292	144
^{46}Sc	889.277 3	99.9840 10	7239456	3456
^{47}Sc	159.381 15	68.3 4	289370.88	51.84
^{48}Sc	1037.522 12	97.6 7	157212	324
^{48}V	944.130 4	7.780 7	1380110.4	216
^{48}Cr	308.24 6 2	100	77616	108
^{49}Cr	152.928 2	30.3 11	2568	6
^{51}Cr	320.0824 4	9.910 10	2393625.6	259.2
^{42}K	1524.6 3	18.08	44478	25.2
^{43}K	617.490 6	79.2 6	80280	360
^{24}Na	1368.626 5	99.9936 15	53989.2	43.2
^{57}Ni	1377.63 3	81.7 24	128160	216

4.1 The acquisition data procedure

The gamma-spectrometry of both monitor and target foils was performed using a HPGe detector. The strategy adopted consists in a first fast acquisition, lasted typically 10-15 minutes and performed starting from about 3 hours after the EOB (End Of Bombardment), of all the target foils. In the following days, longer acquisitions were made, of about 2-3 hours each, in order to follow the decay of the produced radionuclides. One more spectrum for each foil is collected at a distance of 2-3 months, in conjunction with a new irradiation run, in order to measure the activity of the long-lived radioisotopes, such as ^{46}Sc . In the end, at least 5 gamma-spectra acquisitions are obtained for each ^{nat}V foil.

The choice of the first fast acquisition is to be sure to measure also the fast decaying co-produced contaminants, such as ^{49}Cr . Meanwhile, the acquisition of more than one spectrum for each foil allows to reduce the final uncertainties associated to the cross section values, since a weighted average is performed.

Concerning the monitor foils the approach is different. The reactions

considered are $^{27}\text{Al}(\text{p,x})^{24}\text{Na}$ for the first three irradiation runs, where the beam energy was above 40 MeV, and $^{nat}\text{Ni}(\text{p,x})^{57}\text{Ni}$ for the last three irradiation runs, where, instead, the proton energy was below 40 MeV. This selection is a consequence of the cross section values reported in the IAEA recommended reactions list for the two reactions considered, in the energy range investigated in this work (26-70 MeV) [18]: at low energies ^{57}Ni has higher production cross section values than ^{24}Na , and viceversa. Considering the purpose of monitor reactions, the spectrum acquisition is performed only once for each monitor foil.

4.2 Analysis operations

The spectra acquired can be analyzed thanks to the help of an analysis program, called *jRadView*. This application allows, through a proper channel-energy calibration, to have the number of counts as a function of energy of the γ -ray emitted by the radioactive nucleus. Different tools are available to select manually the Gaussian peaks and the background regions in the spectrum. The selection of the peaks follows some basic rules. The ideal peak to choose should be a not shared gamma-peak, with an intensity (probability of a γ emission at a given γ energy) high enough to make the peak visible over the background. Sometimes, it can happen that the most intense peak, generated by a radionuclide, has the contribution of one or more other radionuclides that emit a gamma-ray at the same or at a similar energy; in these cases the choice of another peak, if possible, is more appropriate. This is not possible for the case of ^{43}Sc , for example, since it has only one gamma-peak at 373 keV, reported in table 4.1, generated also by ^{43}K ($E_\gamma=372.760$ keV, $I=86,80\%$). The only possibility, in this case, is to perform a correction of the ^{43}K contribution, on the 373 keV γ -peak, to obtain the ^{43}Sc activity. After selection, is performed an integral which returns the area underlying each peak corrected from the background, corresponding to the number of counts forming that peak. In figure 4.1 there is an example of the described procedure of selection; the corresponding results returned by *jRadView* in the results window are presented in figure 4.2.

Among the values returned by *jRadView* and reported in figure 4.2, the numbers of counts, resulting from the integral, are called *Area* (*dArea* is its associated error useful for uncertainties calculation). Those values are the key of the cross section values calculations, performed through the equation proposed by Otuka et al. [19]:

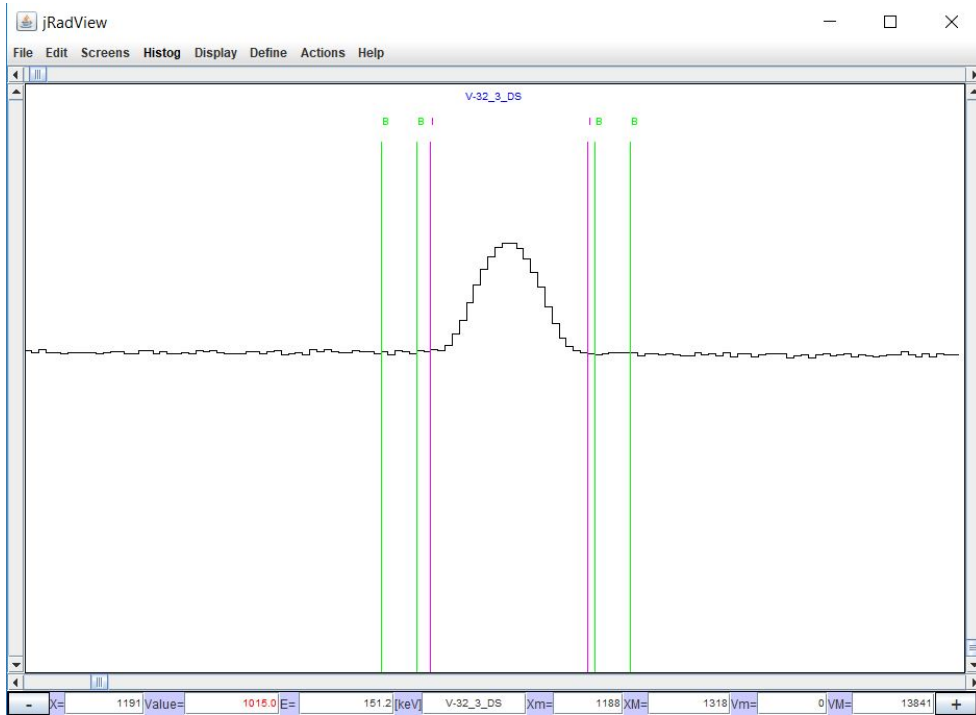


Figure 4.1: Example of how are made the selections concerning a peak. This peak in particular belongs to ^{47}Sc .

$$\sigma_x = \sigma_r \frac{C_x n_r \epsilon_r I_r f_r}{C_r n_x \epsilon_x I_x f_x} \quad (4.1)$$

In this equation the subscript x indicates the quantities linked to the radionuclide of interest while the subscript r shows which are the parameters owned by the monitor reactions. In particular, C represents exactly the number of counts just mentioned. Among the other quantities, f is the time factor,

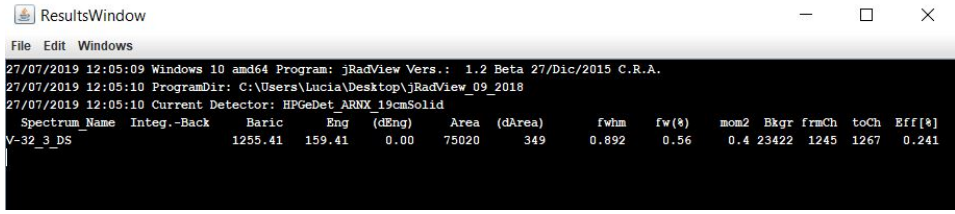


Figure 4.2: Values returned by jRadView corresponding to the previous selections.

equal to:

$$f_x = (1 - e^{-\lambda_x t_i})e^{-\lambda_x t_{c,x}}(1 - e^{-\lambda_x t_{m,x}})/\lambda_x \quad (4.2)$$

where t_i is the irradiation time, $t_{c,x}$ is the cooling time and $t_{m,x}$ is the measurement time, while λ_x is the decay constant (for the monitor radionuclide time factor the x should be substituted by the r). The irradiation time, t_i , is the same for all the spectra acquired and it lasts roughly one hour. The cooling time, $t_{c,x}$, is the time elapsed between the EOB and the spectrum acquisition and it is different for each spectrum. Its value can range from some hours to some months. The measurement time, $t_{m,x}$, is the measurement real time, so it includes the dead time of the detector. Its value can be of some minutes, for the first fast acquisitions, as well as of some hours in longer acquisitions. The decay constants, λ , come from NuDat [17]. More precisely, the decay constants are obtained as $\lambda = 1/T_{1/2}$, where $T_{1/2}$ are the values tabulated in the database and reported in table 4.1. Another quantity in the equation (4.1) is σ_r . It is the cross section value of the monitor reaction, assumed at a beam energy equal to that in the monitor foil, reported in Appendix A, taken from the IAEA list of recommended reactions [18]. Then there is the radiation intensity I : it is get from the National Nuclear Data Center (NNDC) [17]. Concerning the quantity n , it is determined by target characteristics and is calculated as

$$n = \frac{\rho P x N_A}{A} \quad (4.3)$$

where ρ is the density, P is the purity, x is the thickness, N_A is the Avogadro number and A is the number mass of the target. The last quantity is the efficiency ϵ . The value to use in the equation is returned by the *jRadView* program itself. This value, called *Eff[%]* in the results window reported in figure 4.2, is calculated through the equation 3.9 with the coefficients reported in table 3.3, in the previous chapter.

An important aspect to consider, when calculating the number of counts, is the recoil effect, described in Chapter 3. When observing the spectra of a target foil and its following monitor foil, it is possible to observe in the monitor foil spectrum some unexpected peaks generated by γ -emissions of radionuclides produced in the target foil, as a consequence of the recoil effect. The counts in the monitor foil have to be associated to the corresponding peak in the target foil to have the real number of counts. The same is true when the position of the target and monitor foils is inverted.

The analysis process is completed with the computation of the uncertainties. Formulas used for this aim are presented always in the same paper by Otuka et al. [19]. The uncertainty for the equation (4.1) is:

$$\left(\frac{\Delta\sigma_x}{\sigma_x}\right)^2 = \sum_q \left(\frac{\Delta q_x}{q_x}\right)^2 + \sum_q \left(\frac{\Delta q_r}{q_r}\right)^2 + \left(\frac{\Delta\sigma_r}{\sigma_r}\right)^2 \quad (4.4)$$

where the subscripts x and r mean always studied and monitor reactions respectively and $q = C, n, \epsilon, I, f$ represents in turn all the parameters. $\frac{\Delta n}{n}$ and $\frac{\Delta\epsilon}{\epsilon}$ are assumed to be 0.5% and 5% respectively. The error on the intensity ΔI is taken from the NuDat database [17] and reported in table 4.1. For C and f the situation is a little more complicated. The uncertainty in the time factor is the propagation from the uncertainty in the decay constant, namely

$$\left(\frac{\Delta f}{f}\right)^2 = s_{f\lambda}^2 \left(\frac{\Delta\lambda}{\lambda}\right)^2 \quad (4.5)$$

with $f = f_x$ or f_r and $\lambda = \lambda_x$ or λ_r , and where the relative sensitivity $s_{f\lambda}$ is

$$s_{f\lambda} = \frac{\lambda}{f} \frac{\partial f}{\partial \lambda} = \left(\frac{\lambda t_i e^{-\lambda t_i}}{1 - e^{-\lambda t_i}} - \lambda t_c + \frac{\lambda t_m e^{-\lambda t_m}}{1 - e^{-\lambda t_m}} - 1 \right). \quad (4.6)$$

The result is nothing less than the error propagation for the equation (4.2). The uncertainty on decay constants is always deduced from the $dT_{1/2}$ tabulated in the NuDat database and reported in table 4.1. At first sight the uncertainty of the number of counts may seem easy. The jRadView interface returns the value $dArea$, as anticipated previously in this chapter, which represents the error of the $Area$ so of the number of counts. Consequently $dArea$ seems exactly the desired ΔC . But this is not true because the two possible corrections on the number of counts mentioned before, due to the recoil effect and to the possibility of common peaks, should be taken into account even in the uncertainties calculation. To add those contribution to $dArea$ the error propagation is simply used. The values corrected are then inserted as the ΔC s required in the equation (4.4).

In table 4.1 it is possible to notice that some intensity values have not their corresponding uncertainty. This is the case of ^{48}Cr for example. In this situation the term corresponding to the intensity in the equation (4.4) for the uncertainty computation is neglected. Examining always the intensity column the attention falls on the small intensity of ^{48}V . The choice is guided by the fact that ^{48}V and ^{48}Sc share the majority of the more intense peaks. The 944 keV peak is the first free ^{48}V peak with, fortunately, an adequate intensity.

4.2.1 The case of ^{44m}Sc and ^{44g}Sc

A different matter is the case of ^{44}Sc isotope. This is because this isotope has a metastable and a ground states. The ^{44m}Sc decay contributes to increase the ^{44g}Sc population which in conclusion has one component directly produced during bombardment and another one due to the decay of the metastable state. So while the metastable state cross section is easily calculated starting from its unshared 271.241 keV γ -line, the ground state has only one suitable peak enough intense ($I = 99.9\%$) to be seen in the spectrum at 1157.020 keV. However this peak is generated also by ^{44m}Sc with less intensity (1157.002 keV, $I = 1.20\%$). In conclusion 1157 keV γ -line number of counts is composed by the γ emissions of: the metastable state, the directly produced ^{44g}Sc and the ground state originated by the isomeric transition of the ^{44m}Sc , with an isomeric transition coefficient equal to $b_{IT} = 98.80\%$. The equation used to compute ^{44g}Sc cross section is thus a function of C_{271} and C_{1157} numbers of counts [19]

$$\sigma_g = \frac{1}{n\phi I_{1157,g} f_g} \left[\frac{C_{1157}}{\epsilon_{1157}} - \frac{C_{271}}{\epsilon_{271}} \frac{I_{1157,m}}{I_{271}} - \frac{C_{271}}{\epsilon_{271}} \frac{b_{IT} I_{1157,g}}{I_{271} f_m} \frac{\lambda_m \lambda_g}{\lambda_m - \lambda_g} \left(\frac{f_g}{\lambda_g} - \frac{f_m}{\lambda_m} \right) \right] \equiv \alpha (\beta - \gamma - \delta) \quad (4.7)$$

where clearly m and g indicate metastable and ground states respectively. The Greek letters α , β , γ and δ are used exclusively to rewrite the formula in a cleaner way. The only new parameter is ϕ , that describes the number of incident particles per irradiation time and it is not directly measurable by definition. ϕ can be derived from the cross section definition considering monitor reaction

$$\sigma_r = \frac{C_r}{n_r \phi \epsilon_r I_r f_r}. \quad (4.8)$$

Here all parameters except ϕ are known.

The uncertainty to associate to the ^{44g}Sc cross section can be obtained from

$$\left(\frac{\Delta \sigma_g}{\sigma_g} \right)^2 = \sum_k s_k^2 \left(\frac{\Delta x_k}{x_k} \right)^2 \quad (4.9)$$

where $x_k = (n, \phi, \epsilon_{1157}, \epsilon_{271}, C_{1157}, C_{271}, I_{1157}, I_{271}, b_{IT})$ and s_k are relative sensitivity coefficients generally defined as

$$s_k = \left(\frac{x_k}{\sigma_g} \right) \left(\frac{\partial \sigma_g}{\partial x_k} \right) \quad (4.10)$$

which in the case of ^{44g}Sc take the explicit forms

$$\left(\frac{n}{\sigma_g} \right) \left(\frac{\partial \sigma_g}{\partial n} \right) = 1 \quad \left(\frac{\phi}{\sigma_g} \right) \left(\frac{\partial \sigma_g}{\partial \phi} \right) = 1$$

$$\left(\frac{\epsilon_{1157}}{\sigma_g} \right) \left(\frac{\partial \sigma_g}{\partial \epsilon_{1157}} \right) = -\frac{\alpha\beta}{\sigma_g} \quad \left(\frac{\epsilon_{271}}{\sigma_g} \right) \left(\frac{\partial \sigma_g}{\partial \epsilon_{271}} \right) = \frac{\alpha}{\sigma_g} (\gamma + \delta)$$

$$\left(\frac{C_{1157}}{\sigma_g} \right) \left(\frac{\partial \sigma_g}{\partial C_{1157}} \right) = \frac{\alpha\beta}{\sigma_g} \quad \left(\frac{C_{271}}{\sigma_g} \right) \left(\frac{\partial \sigma_g}{\partial C_{271}} \right) = -\frac{\alpha}{\sigma_g} (\gamma + \delta)$$

$$\left(\frac{I_{1157,g}}{\sigma_g} \right) \left(\frac{\partial \sigma_g}{\partial I_{1157,g}} \right) = -\frac{\alpha}{\sigma_g} (\beta - \gamma) \quad \left(\frac{I_{271}}{\sigma_g} \right) \left(\frac{\partial \sigma_g}{\partial I_{271}} \right) = \frac{\alpha}{\sigma_g} (\gamma + \delta)$$

$$\left(\frac{b_{IT}}{\sigma_g} \right) \left(\frac{\partial \sigma_g}{\partial b_{IT}} \right) = -\left(\frac{\alpha\delta}{\sigma_g} \right)$$

It should be specified that similarly to the other isotopes also in ^{44}Sc case the recoil effect has to be considered and consequently both the cross section and its uncertainty corrected. On the other hand the effect of being a common peak is just included in previous equations.

At the end of all the procedure exposed different cross section values with the associated errors are available for each isotope in each foil employed in one of the six irradiation runs, basically those values correspond to the same energy. To obtain a single cross section measure with its single uncertainty a weighted average is performed. The errors themselves are selected as weights. This additional step has a favorable effect of reducing the uncertainties paired with the cross sections.

4.3 Calculation of the cross section energy values

The results are presented in a radioisotope cross section versus proton energy graph. So it is essential to know which is the corresponding proton energy. Because of the proton beam crosses several layers of different materials before

reaching each foil, such as insulating kapton foils, air and sometimes degraders, the proton energy is no more the nominal one configured in the cyclotron because protons lose energy in a medium according to Bethe-Bloch formula. The apparatus is not able to measure the energy in any point of the target so it needs to be deduced through a simulation. For this aim is exploited the SRIM software [20]. Thanks to this tool it is possible to simulate the particle energy loss throughout nuclear reactions occurring in an irradiated target. Its advantage is the free choice regarding the type of beam, its initial energy and number of particles; moreover it requires the target construction specifying the material, the thickness and the physical state. The software results contain different informations between which there is the energy of each particle created. The final useful energy would be the average of all those single energies.

When the target is done, including the kapton foil and the air layer, a proton beam of 1000 particles is selected, with a different energy for each irradiation. 1000 particles correspond to the minimum number above which the returned foil energy remains stable. The problem is that in a real situation it is impossible to know where exactly the reaction took place in the foil and the energy corresponding at that position. As reasonable approximation, it is adopted, as energy value, the one in the middle of each foil, estimated as the average between the one obtained at the end of the considered foil and the one at the beginning of the same foil. Two more simulations are performed to take into consideration the energy straggling, one adding and one subtracting 500 keV to the initial energy. The error to associate to the final energy value is obtained through the standard deviation, since the energy loss is a statistical process.

The final energy values with their uncertainties, derived from simulations, are used to represent the cross section values obtained, in the graphs reported in the next chapter.

Chapter 5

Presentation of the results

The aim of this Chapter is to present and discuss the production cross sections of all the radionuclides involved in proton-induced reactions on a ^{nat}V target. Those values are useful to understand which are the radioisotopes generated and which is the probability of their production at different proton energies. The collected informations are a first step towards the study of new radiopharmaceuticals for medical applications, based on the use of the theranostic radionuclide ^{47}Sc .

5.1 Cross sections of all the radionuclides produced by $^{nat}\text{V}(\text{p},\text{x})$ reactions

Six irradiation runs were performed at ARRONAX facility, using the tunable (34-70 MeV) low current (100 nA) proton beam and stacked-foil targets. Thin ^{nat}V foils (purity > 99.8 %, thickness = 20 μm) were separated by thick aluminium foils, used as beam degrader. In the first four irradiation runs three Vanadium foils were inserted in the stacked-foil target, while in the last two runs the foil only one ^{nat}V target was included. Since from each ^{nat}V foil it is possible to measure a cross section at the corresponding proton energy, 14 values may be totally obtained at different proton energies. However, some radionuclide are not produced in some specific energy ranges or can not be distinguished from the background due to their low intensity γ -rays: in those cases, less cross section values can be measured, as reported on the following tables and graphs.

The results obtained are presented and discussed below.

The natural Vanadium is composed by both ^{51}V and ^{50}V (^{51}V 99.750%; ^{50}V 0.250%), so the results can be attributed mostly to the ^{51}V contribution. However the results obtained in this thesis refer to ^{nat}V targets.

5.1.1 ^{48}Cr production

The reactions contributing to ^{48}Cr production are namely $^{51}\text{V}(p,4n)^{48}\text{Cr}$ and $^{50}\text{V}(p,3n)^{48}\text{Cr}$. It then decays via ε mode, so through an electron capture (EC) followed by a β^+ emission, with a probability of 100% [21].

The production cross section results are reported in table 5.1.

Table 5.1: Numerical values for ^{48}Cr production cross section from ^{nat}V targets.

Energy		^{48}Cr	
E(MeV)	dE(MeV)	$\sigma(\text{mb})$	$d\sigma(\text{mb})$
70.0	0.5	1.14	0.05
67.8	0.7	1.28	0.06
65.5	0.8	1.40	0.06
60.7	0.5	1.67	0.14
58.3	0.7	1.87	0.09
55.7	0.8	1.87	0.09
53.6	0.6	1.74	0.08
50.9	0.7	1.46	0.08
48.1	0.8	1.04	0.05
39.5	0.6		
33.3	0.6		
31.2	0.7		
29.2	0.7		
26.5	0.8		

The last cross section values of table 5.1 are missing because in the spectra corresponding to those proton energies the ^{48}Cr peak is not visible. Probably at such low energies ^{48}Cr is no longer produced.

Results reported in table 5.1 are also shown on the plot in figure 5.1. In the energy range selected it can be seen that the activation cross section values are low (always below 2 mb) and that the maximum is around 58 MeV.

5.1.2 ^{49}Cr production

For the ^{49}Cr case the two possible reactions involved in the ^{49}Cr production are $^{51}\text{V}(p,3n)^{49}\text{Cr}$ and $^{50}\text{V}(p,2n)^{49}\text{Cr}$. Once it is created its decay mode is a

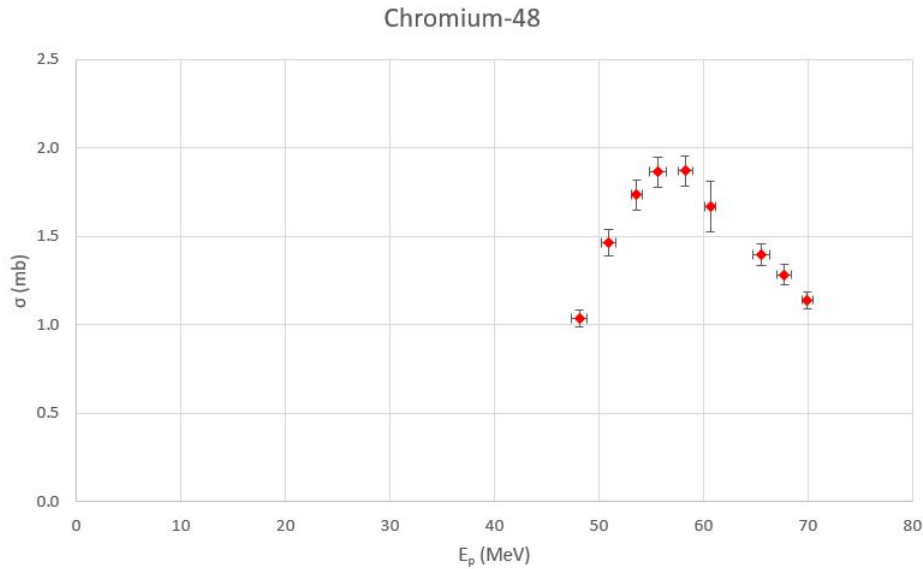


Figure 5.1: Cross section values as a function of the proton energy for ^{48}Cr production.

β^+ emission in the 100% of the cases.

The cross section values obtained for ^{49}Cr are reported in table 5.2 and shown in figure 5.2.

Looking at table 5.2, it can be noticed that the errors associated to cross section values are larger if compared to the errors obtained for the majority of the other isotopes. The reason is that ^{49}Cr is a relatively fast decaying isotope ($T_{1/2} = 42.3$ min) so only in the first foils' spectra, shortly acquired after the EOB, the ^{49}Cr γ -ray can be used for the cross section calculation. In the later measurements the ^{49}Cr is almost decayed. In conclusion, there are not enough values to perform the weighted average which induces the error reduction.

The figure 5.2 shows a rapid cross section increase with energy, in the range considered, with a maximum probably near 40 MeV.

5.1.3 ^{51}Cr production

The ^{51}Cr production is due to the two possible reactions $^{51}\text{V}(p,n)^{51}\text{Cr}$ and $^{50}\text{V}(p,\gamma)^{51}\text{Cr}$. After production it decays via ε mode.

Measured cross section values are reported in table 5.3 and the data are then arranged in figure 5.3.

The ^{51}Cr cross section as a function of proton energy has a different

Table 5.2: Numerical values for ^{49}Cr production cross section from ^{nat}V targets.

Energy		^{49}Cr	
E(MeV)	dE(MeV)	$\sigma(\text{mb})$	$d\sigma(\text{mb})$
70.0	0.5	6.17	0.54
67.8	0.7	6.85	0.63
65.5	0.8	7.13	0.66
60.7	0.5	8.90	1.23
58.3	0.7	10.23	0.78
55.7	0.8	10.83	0.82
53.6	0.6	11.98	1.29
50.9	0.7	14.12	1.52
48.1	0.8	17.86	1.85
39.5	0.6	27.72	2.64
33.3	0.6	24.38	2.43
31.2	0.7	16.24	1.55
29.2	0.7	6.77	0.65
26.5	0.8	0.66	0.07

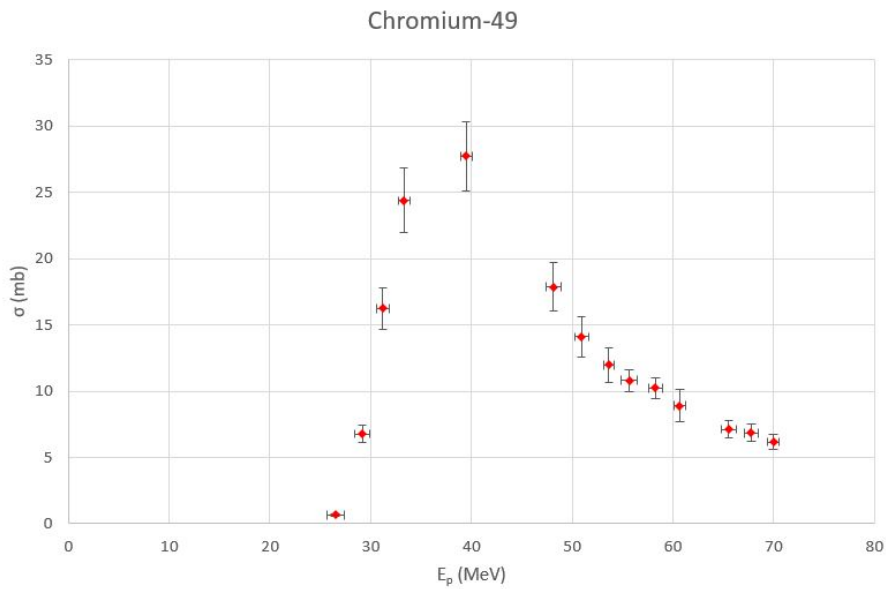


Figure 5.2: Cross section values as a function of the proton energy for ^{49}Cr production.

Table 5.3: Numerical values for ^{51}Cr production cross section from ^{nat}V targets.

Energy		^{51}Cr	
E(MeV)	dE(MeV)	$\sigma(\text{mb})$	$d\sigma(\text{mb})$
70.0	0.5	10.7	0.6
67.8	0.7	11.9	0.7
65.5	0.8	12.2	0.6
60.7	0.5	16.8	1.8
58.3	0.7	18.4	1.1
55.7	0.8	18.5	1.1
53.6	0.6	16.4	1.0
50.9	0.7	17.4	1.0
48.1	0.8	18.9	1.0
39.5	0.6	24.6	1.3
33.3	0.6	33.9	1.4
31.2	0.7	33.3	1.4
29.2	0.7	33.0	1.3
26.5	0.8	45.1	1.8

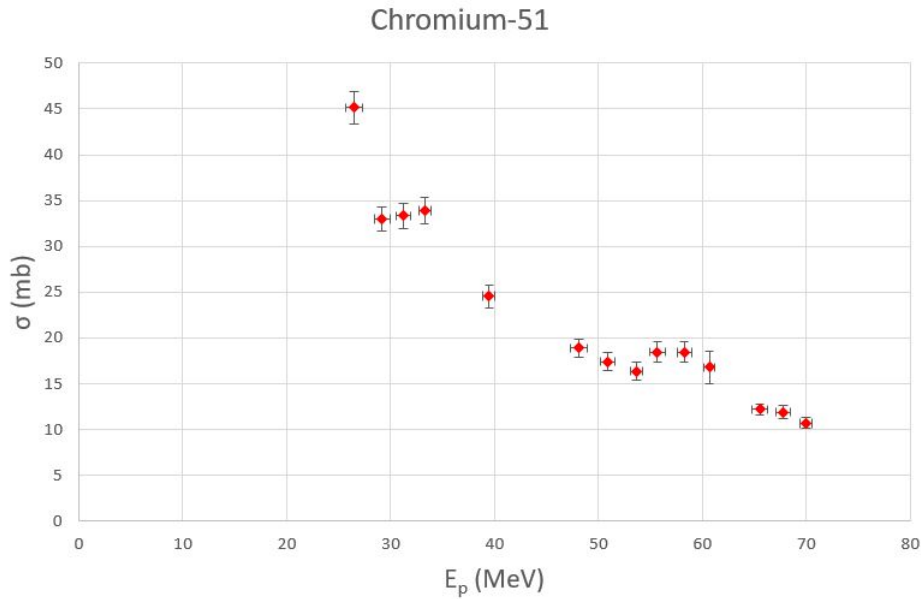


Figure 5.3: Cross section values as a function of the proton energy for ^{51}Cr production.

trend compared to all the other isotopes. At low energies the cross section is larger than at high energies. This means that the production has a higher probability to occur at low energies. It can be also noticed that the cross section decreasing trend is not so uniform but it reveals some fluctuations.

5.1.4 ^{48}V production

The ^{48}V activation cross section is cumulative, meaning that ^{48}V formation is due both to the direct production by the reactions listed in Appendix B and to the indirect production coming from the decay of its parent isotope ^{48}Cr ($T_{1/2} = 21.56$ h). ^{48}V decay mode is of the ε type.

The cross section values measured are tabulated in table 5.4 and then displayed in figure 5.4.

From figure 5.4 is possible to identify a region around 55 MeV inside the energy range investigated where the ^{48}V production cross section is maximized. Among all the isotopes ^{48}V is also the one which reaches the greatest cross section values.

Table 5.4: Numerical values for ^{48}V production cross section from ^{nat}V targets.

Energy		^{48}V	
E(MeV)	dE(MeV)	$\sigma(\text{mb})$	$d\sigma(\text{mb})$
70.0	0.5	71.34	3.01
67.8	0.7	77.62	3.24
65.5	0.8	78.44	3.28
60.7	0.5	90.06	7.42
58.3	0.7	101.10	4.52
55.7	0.8	102.35	4.56
53.6	0.6	101.25	4.71
50.9	0.7	90.34	4.22
48.1	0.8	73.27	3.30
39.5	0.6	7.99	0.53
33.3	0.6	2.13	0.11
31.2	0.7	1.22	0.06
29.2	0.7	0.40	0.02
26.5	0.8	0.13	0.01

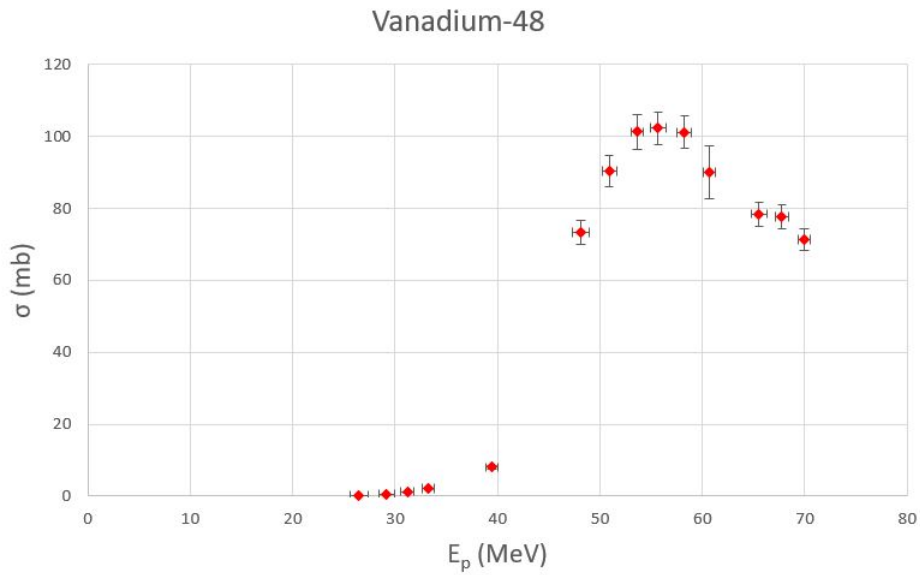


Figure 5.4: Cross section values as a function of the proton energy for ^{48}V production.

5.1.5 ^{43}Sc production

^{43}Sc is a particular case. As ^{48}V , it has a cumulative cross section which is a combination of the direct production contribution, given by the reactions reported in Appendix B, and of the indirect one due to the possible decay of ^{43}Ti , which has a short half-life ($T_{1/2} = 509$ ms). The ^{43}Sc production channel through the production of ^{43}Ti is opened only at higher energies of the energy range investigated. Once produced ^{43}Sc decays through ε mode.

Table 5.5: Numerical values for ^{43}Sc production cross section from ^{nat}V targets.

Energy		^{43}Sc	
E(MeV)	dE(MeV)	$\sigma(\text{mb})$	$d\sigma(\text{mb})$
70.0	0.5	0.36	0.05
67.8	0.7	0.34	0.06
65.5	0.8	0.08	0.06
60.7	0.5		
58.3	0.7		
55.7	0.8	0.04	0.02
53.6	0.6	0.09	0.04
50.9	0.7		
48.1	0.8	0.45	0.24
39.5	0.6		
33.3	0.6		
31.2	0.7		
29.2	0.7		
26.5	0.8		

The anomaly of ^{43}Sc production cross sections can be observed in the data listed in table 5.5 and shown in figure 5.5. It can be noticed, from the lack of data in some rows of table 5.5, the impossibility to determine ^{43}Sc cross section in some spectra. Moreover the uncertainties associated are rather high. The reason is that ^{43}Sc has only one available peak ($E_\gamma = 372.9$ keV, $I = 22.5$ %) and this peak is in common with another isotope, ^{43}K ($E_\gamma = 372.760$ keV, $I = 86.80$ %), as anticipated in the previous chapter in table 4.1. The method to determine the ^{43}K contribution to the 373 keV peak starts from the calculation of ^{43}K activity from 617 keV peak, that presents no interference with other gamma-rays in the spectra. From ^{43}K activity is possible to

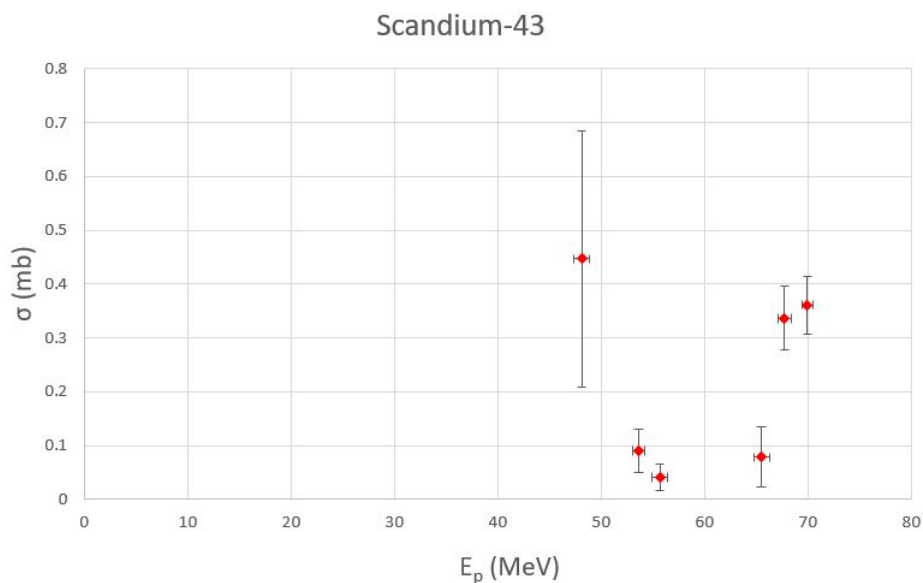


Figure 5.5: Cross section values as a function of the proton energy for ^{43}Sc production.

calculate the number of counts due to ^{43}K in the 373 keV gamma-line and thus, by subtraction, the true number of counts due to ^{43}Sc . This is the reason why the ^{43}Sc cross section values calculated present larger uncertainties than other radionuclides studied in the thesis work. Moreover, the relatively short half-life of ^{43}Sc ($T_{1/2}=3.891$ h) makes this radionuclide detectable only in the first two spectra acquired post the EOB. This contributes to the effect of reducing uncertainties of weighted average. Differently, ^{43}K has a longer half-life ($T_{1/2}=22.3$ h) so, in the spectra acquired longer after the EOB, the 373 keV peak is only due to the ^{43}Sc emission, as confirmed by the activity calculation performed with the 617 keV γ -ray.

The trend of ^{43}Sc cross section is fluctuating, as reported in figure 5.5, because the energy range investigated covers the threshold energy. In particular, the lowest energy value with large uncertainty ($\sim 50\%$) is reported for completeness but probably the production cross section of ^{43}Sc starts at $E_p > 50$ MeV.

5.1.6 ^{44m}Sc production

^{44m}Sc is the metastable state of the ^{44}Sc radionuclide. It is directly produced through the reactions listed in Appendix B and indicated generally as the reactions of the ^{44}Sc isotope. ^{44m}Sc decays with a probability of 98.80 %

through an isomeric transition (IT) while the remaining 1.20 % probability is for electron capture followed by β^+ emission, so for ε decay mode. The isomeric transition generates the ^{44g}Sc state of this isotope.

The ^{44m}Sc cross section values are reported in table 5.6 and graphically presented in figure 5.6.

Table 5.6: Numerical values for ^{44m}Sc production cross section from ^{nat}V targets.

Energy		^{44m}Sc	
E(MeV)	dE(MeV)	$\sigma(\text{mb})$	$d\sigma(\text{mb})$
70.0	0.5	8.08	0.32
67.8	0.7	7.09	0.30
65.5	0.8	5.32	0.23
60.7	0.5	1.93	0.17
58.3	0.7	1.03	0.05
55.7	0.8	0.45	0.02
53.6	0.6	0.24	0.01
50.9	0.7	0.13	0.01
48.1	0.8	0.05	0.01
39.5	0.6		
33.3	0.6		
31.2	0.7		
29.2	0.7		
26.5	0.8		

Figure 5.6 and table 5.6 show that, in the energy range investigated, energy value at which ^{44m}Sc starts to be produced with a certain probability is around 48 MeV.

5.1.7 ^{44g}Sc production

The other isomeric state of ^{44}Sc is the ground state. ^{44g}Sc can be produced directly through the same proton activated reactions available for ^{44m}Sc production, shown in Appendix B, and indirectly through the decay of the metastable state, but also the decay of its parent nucleus ^{44}Ti . ^{44}Ti has a really long half-life ($T_{1/2} = 60.0$ y) so its contribution to ^{44g}Sc formation can be neglected since the irradiation time (about 1 hour) can eventually produce a very small amount of ^{44}Ti ; moreover, the decay time after the EOB

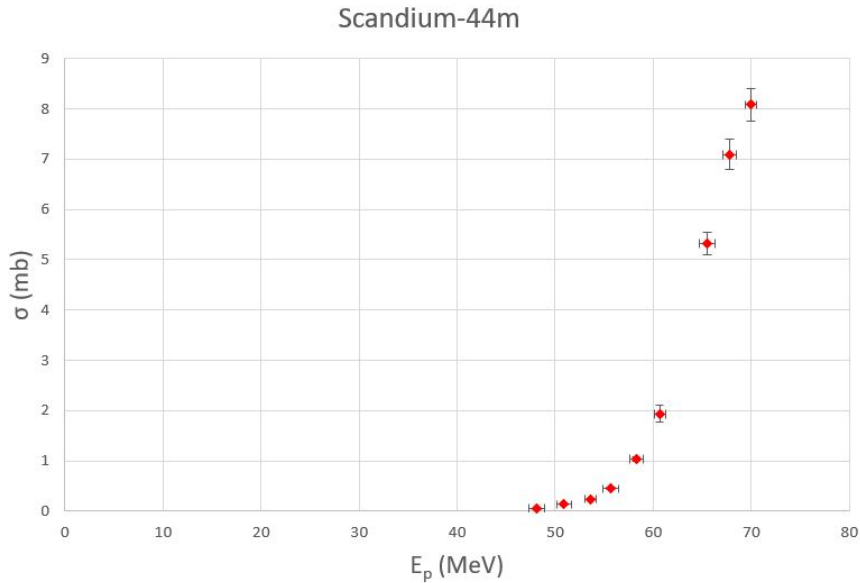


Figure 5.6: Cross section values as a function of the proton energy for ^{44m}Sc production.

when the spectra are acquired (up to 5 days) is negligible in comparison with the half-life of ^{44}Ti . The decay mode of ^{44g}Sc is a pure ϵ .

In table 5.7 are indicated the production cross section values. It should be recalled that ^{44g}Sc cross section calculation requires separate equations, explicated in the previous chapter, which take into account the corrections for the ^{44m}Sc contribution. The values obtained are then presented in figure 5.7.

The ^{44g}Sc cross section trend in figure 5.7 shows similar features to ^{44m}Sc . It is not strange since they are two isomeric state of the same radionuclide. The uncertainty value of ^{44g}Sc are larger than the ^{44m}Sc case, since they also include the correction factor for ^{44m}Sc contribution.

5.1.8 ^{46}Sc production

The main contribution to ^{46}Sc cross section comes from the reactions mentioned in Appendix B. The other minor competitor is the fast decay of its isomeric state ($T_{1/2} = 18.75$ s). Differently from the ^{44}Sc case, the isomeric state is not a problem because when the spectra are measured, about 3 hours after the EOB, the ^{46m}Sc is almost vanished. Once produced ^{46}Sc decays emitting a β^- particle.

The cross section values are given in table 5.8 followed by the graphical

Table 5.7: Numerical values for ^{44g}Sc production cross section from ^{nat}V targets.

Energy		^{44g}Sc	
E(MeV)	dE(MeV)	$\sigma(\text{mb})$	$d\sigma(\text{mb})$
70.0	0.5	8.78	0.62
67.8	0.7	7.47	0.60
65.5	0.8	5.63	0.47
60.7	0.5	2.13	0.25
58.3	0.7	1.15	0.08
55.7	0.8	0.58	0.04
53.6	0.6	0.36	0.03
50.9	0.7	0.15	0.04
48.1	0.8	0.16	0.04
39.5	0.6		
33.3	0.6		
31.2	0.7		
29.2	0.7		
26.5	0.8		

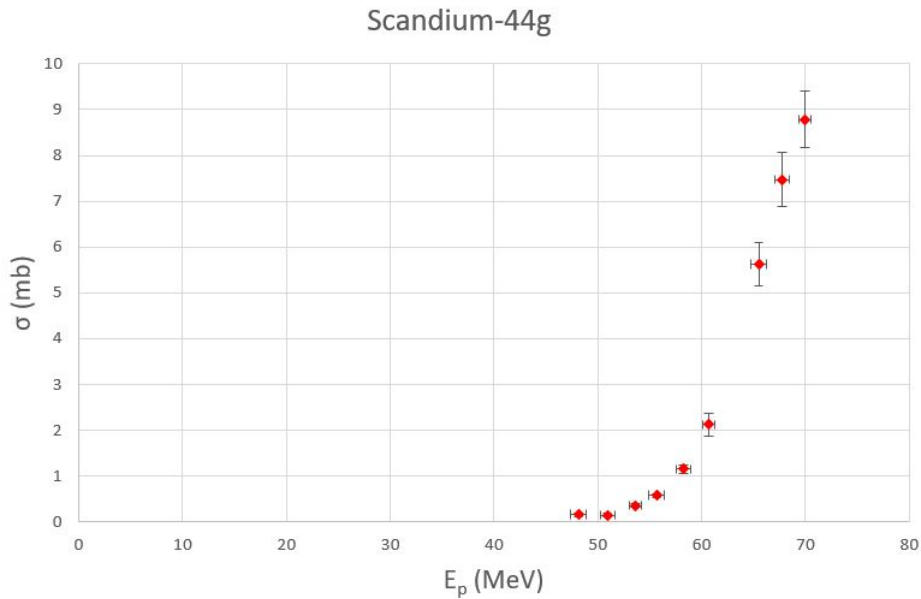


Figure 5.7: Cross section values as a function of the proton energy for ^{44g}Sc production.

representation in figure 5.8.

The ^{46}Sc cross section behavior is particularly important because it is the ^{47}Sc major isotopic contaminant for its really long half-life ($T_{1/2} = 83.79$ d), as mentioned before. From this point of view it is helpful to define a possible energy where ^{46}Sc starts to be produced and to establish at which energy the maximum cross section value is reached. From figure 5.8 the beginning of ^{46}Sc production can be located around $E_p = 30$ MeV while the maximum is between 40 MeV and 48 MeV. With the help of table 5.8 it can be added that the cross section maximum value is at least larger than 30 mb.

5.1.9 ^{47}Sc production

The nuclear reactions involved in the ^{47}Sc formation are listed in Appendix B. ^{47}Sc is a β^- emitter ($T_{1/2} = 3.3492$ d) so it follows the β decay.

The activation cross sections are shown in table 5.9 and the representation is reported in figure 5.9.

The most important consideration on the ^{47}Sc trend in figure 5.9 is that significant production cross section values are identified even at low energies ($E_p < 30$ MeV) in contrast to ^{46}Sc case. Moreover, below 30 MeV, ^{47}Sc cross section values are larger than ^{46}Sc ones. For energies higher than 35 MeV,

Table 5.8: Numerical values for ^{46}Sc production cross section from ^{nat}V targets.

Energy		^{46}Sc	
E(MeV)	dE(MeV)	$\sigma(\text{mb})$	$d\sigma(\text{mb})$
70.0	0.5	16.54	0.67
67.8	0.7	16.61	0.71
65.5	0.8	16.23	0.69
60.7	0.5	19.14	1.85
58.3	0.7	21.03	0.94
55.7	0.8	23.27	1.02
53.6	0.6	25.77	1.22
50.9	0.7	28.29	1.34
48.1	0.8	30.44	1.38
39.5	0.6	18.04	0.82
33.3	0.5	2.60	0.15
31.2	0.7	0.53	0.06
29.2	0.7		
26.5	0.8		

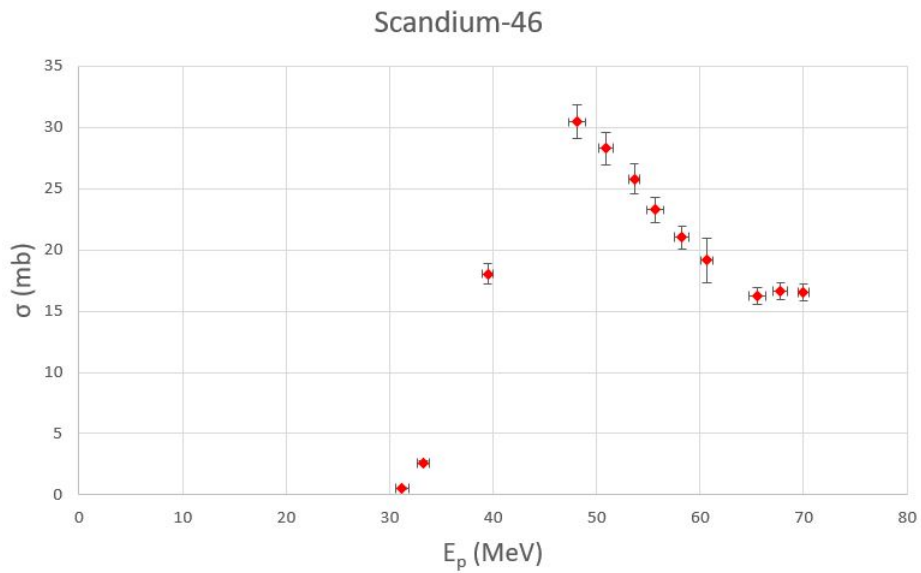


Figure 5.8: Cross section values as a function of the proton energy for ^{46}Sc production.

Table 5.9: Numerical values for ^{47}Sc production cross section from ^{nat}V targets.

Energy		^{47}Sc	
E(MeV)	dE(MeV)	$\sigma(\text{mb})$	$d\sigma(\text{mb})$
70.0	0.5	8.11	0.32
67.8	0.7	7.74	0.33
65.5	0.8	6.82	0.29
60.7	0.5	5.07	0.44
58.3	0.7	4.98	0.23
55.7	0.8	4.41	0.20
53.6	0.6	4.14	0.19
50.9	0.7	4.16	0.19
48.1	0.8	4.51	0.20
39.5	0.6	7.99	0.41
33.3	0.6	11.13	0.49
31.2	0.7	8.85	0.39
29.2	0.7	6.43	0.25
26.5	0.8	4.18	0.18

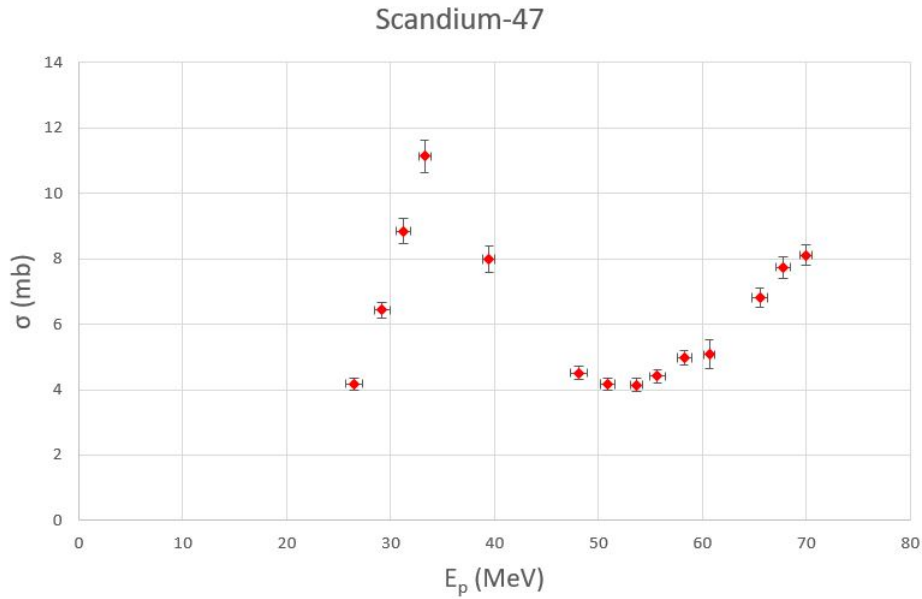


Figure 5.9: Cross section values as a function of the proton energy for ^{47}Sc production.

instead, ^{46}Sc has a higher probability to be produced than ^{47}Sc as can be seen from a comparison between tables 5.8 and 5.9. The ^{47}Sc maximum seems to be in the range between 33 MeV and 39 MeV.

The first peak is due to the reaction $^{51}\text{V}(p,pa)^{47}\text{Sc}$, the first reported in table ???. Above 55 MeV in figure 5.9 can be observed a rise caused by the new channels represented by the other reactions listed in table ???.

In conclusion it is important to underline that a suitable energy range, in which the ^{46}Sc contamination is not present, is up to 30 MeV.

5.1.10 ^{48}Sc production

^{48}Sc can be directly obtained exploiting the reactions reported in Appendix B. ^{48}Sc decay method is always the β^- mode.

The calculated production cross sections are reported in table 5.10. Figure 5.10 has the purpose to illustrate the table 5.10 data.

^{48}Sc production channels are opened starting from about 33 MeV, as can be deduced from observation of table 5.10 and figure 5.10. ^{48}Sc , then, reaches a maximum at roughly 68 MeV and a decreasing trend can be assumed as energy increases.

Table 5.10: Numerical values for ^{48}Sc production cross section from ^{nat}V targets.

Energy		^{48}Sc	
E(MeV)	dE(MeV)	$\sigma(\text{mb})$	$d\sigma(\text{mb})$
70.0	0.5	2.397	0.098
67.8	0.7	2.510	0.110
65.5	0.8	2.353	0.102
60.7	0.5	1.893	0.164
58.3	0.7	1.750	0.082
55.7	0.8	1.405	0.066
53.6	0.6	0.981	0.048
50.9	0.7	0.645	0.034
48.1	0.8	0.376	0.022
39.5	0.6	0.033	0.005
33.3	0.6	0.051	0.008
31.2	0.7		
29.2	0.7		
26.5	0.8		

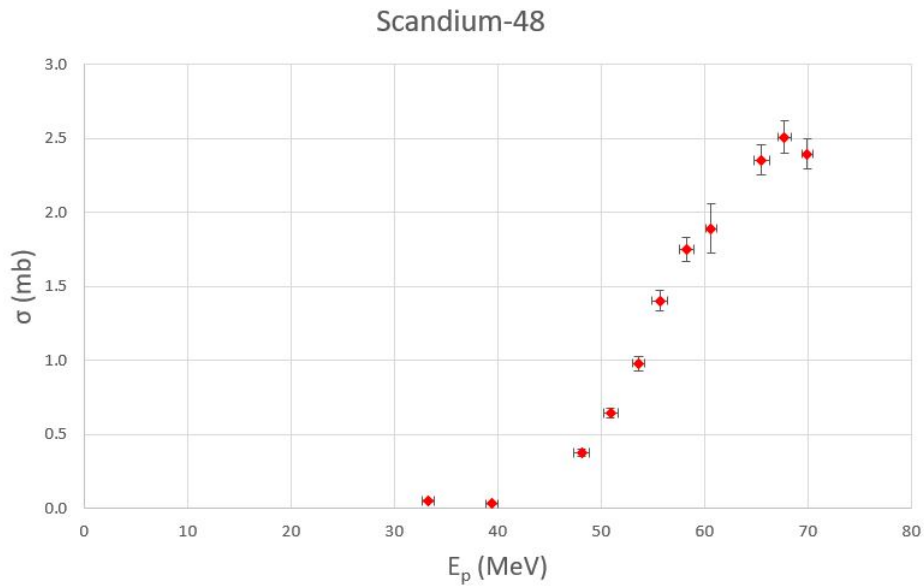


Figure 5.10: Cross section values as a function of the proton energy for ^{48}Sc production.

5.1.11 ^{42}K production

The nuclear reactions responsible for the ^{42}K isotope production in a ^{nat}V target are listed in Appendix B. This isotope decays emitting a β^- particle.

The cross sections values are presented in table 5.11 and in figure 5.11.

Table 5.11: Numerical values for ^{42}K production cross section from ^{nat}V targets.

Energy		^{42}K	
E(MeV)	dE(MeV)	$\sigma(\text{mb})$	$d\sigma(\text{mb})$
70.0	0.5	1.90	0.09
67.8	0.7	2.00	0.10
65.5	0.8	1.72	0.09
60.7	0.5	1.20	0.11
58.3	0.7	0.85	0.05
55.7	0.8	0.50	0.03
53.6	0.6	0.21	0.02
50.9	0.7	0.07	0.01
48.1	0.8		
39.5	0.6		
33.3	0.6		
31.2	0.7		
29.2	0.7		
26.5	0.8		

Looking at the table 5.11 and the figure 5.11 it is clear that the data describes the region where the ^{42}K appears among the products, around 50 MeV. It is highlighted also the presence of a possible maximum, around 68 MeV.

5.1.12 ^{43}K production

^{43}K is essentially produced through the reactions indicated in Appendix B. After formation the decay mode of ^{43}K is β^- .

Table 5.12 presents the activation cross sections measured for ^{43}K by using the 617 keV gamma-line. Results are shown in figure 5.12.

^{43}K cross sections generally show very small values, i.e. below 0.04 mb in the entire energy range investigated. However a maximum value can be find

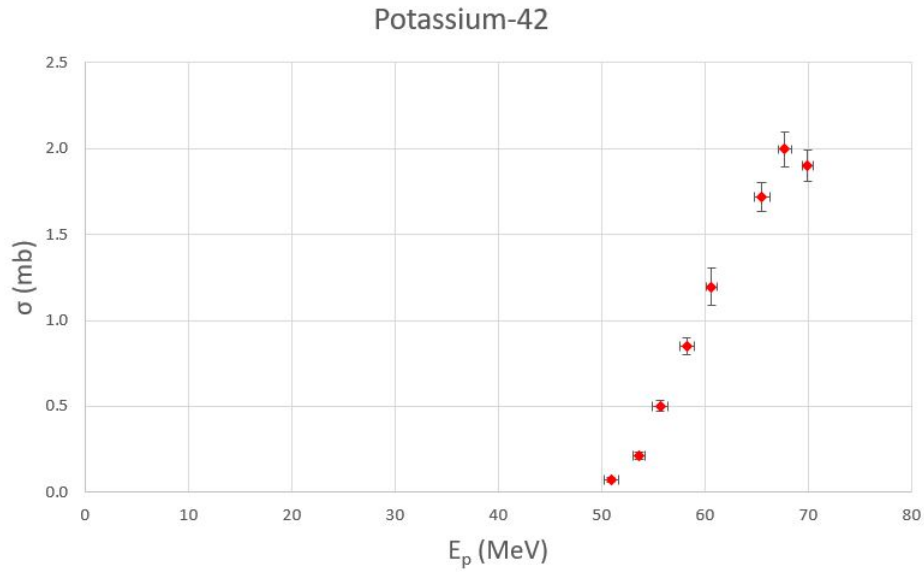


Figure 5.11: Cross section values as a function of the proton energy for ^{42}K production.

Table 5.12: Numerical values for ^{43}K production cross section from ^{nat}V targets.

Energy		^{43}K	
E(MeV)	dE(MeV)	σ (mb)	d σ (mb)
70.0	0.5	0.270	0.014
67.8	0.7	0.280	0.016
65.5	0.8	0.310	0.016
60.7	0.5	0.396	0.035
58.3	0.7	0.438	0.022
55.7	0.8	0.421	0.022
53.6	0.6	0.400	0.023
50.9	0.7	0.333	0.020
48.1	0.8	0.204	0.013
39.5	0.6		
33.3	0.6		
31.2	0.7		
29.2	0.7		
26.5	0.8		

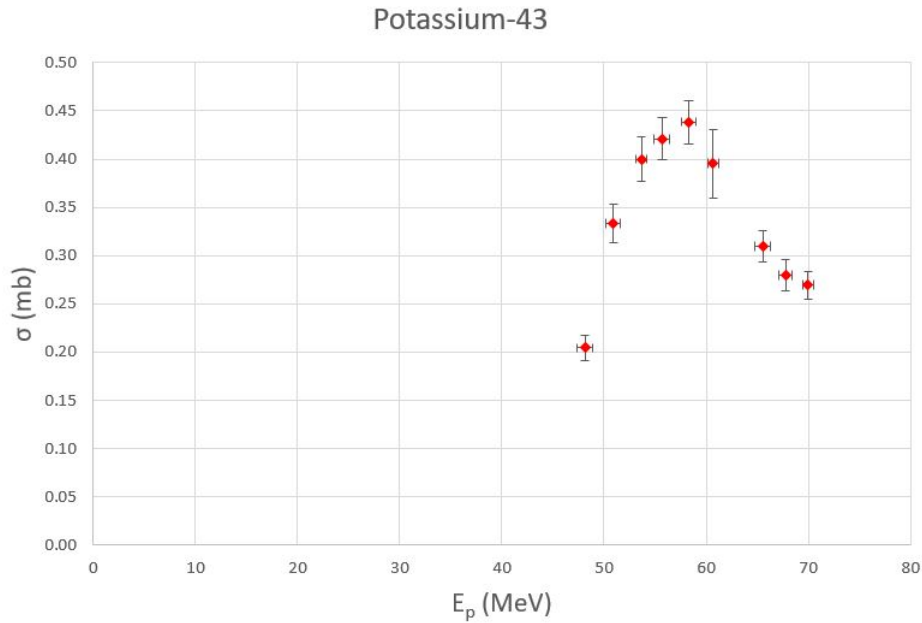


Figure 5.12: Cross section values as a function of the proton energy for ^{43}K production.

around 58 MeV. From figure 5.12 it seems that the probability to produce ^{43}K starts to be influent enough to let the ^{43}K peak be visible in the spectrum at around 48 MeV.

In general it could be noted from figures that in some case having more than one measure in the interval between 33 MeV and 48 MeV could be useful to better describe the cross section trends, for example in ^{46}Sc case the maximum can be better identified. However the results obtained are sufficient to derive the considerations made.

5.2 Comparison of the experimental results with the previous data

The experimental data presented in this work are compared with previous known results, available on the IAEA EXFOR database [22], considering both ^{nat}V and ^{51}V targets.

In the following are reported the $^{nat}\text{V}(p,x)$ reactions results presented in the previous section compared with literature values; a brief discussion is also given.

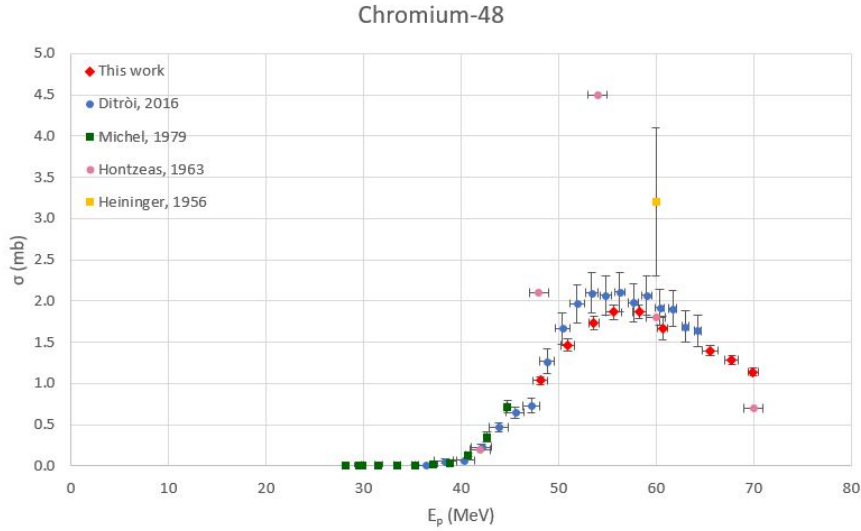


Figure 5.13: Experimental activation cross section results and literature values for $^{nat}\text{V}(p,x)^{48}\text{Cr}$ reactions.

For ^{48}Cr production cross sections obtained in this work are in agreement with the most recent published data by Ditrói et al. [21]. In particular, results shown in this work are smaller than the previous data from 2016. However, considering the error bars, there is agreement on most values. It has to be noted also that the uncertainty values obtained in this work are smaller than the ones previously published thanks to the repeated γ -spectrometry measurements performed for each ^{nat}V foil. The oldest data, instead differ, in particular Hontzeas et al. [23] indicated a maximum more than twice the value of this work while Heiningen et al. [24] presented only a value in this energy range too high despite a really wide error on cross section value. The other reported data from Michel et al. (1979) [25] cover the low energy range where results from this work are not found. Nevertheless in this low energy range the literature data seems to be consistent between them.

In the case of ^{49}Cr , in figure 5.14 are reported, together with the results of figure 5.2, the data from Heiningen, Levkonskij [26], Michel (1979) and Hontzeas. All the previous data differ from the ones presented in this thesis work. A general agreement on the trend of the cross section is noted with results by Michel et al. (1979); however a good agreement with those experimental values is found only up to 31 MeV. Results by Hontzeas (1963) and Heiningen (1956) seem to highly overestimate the trend of this nuclear reaction. It should be reminded that ^{49}Cr is a fast decaying element ($T_{1/2}=42.3$ min) so it can be measured only shortly after the EOB. This could affect

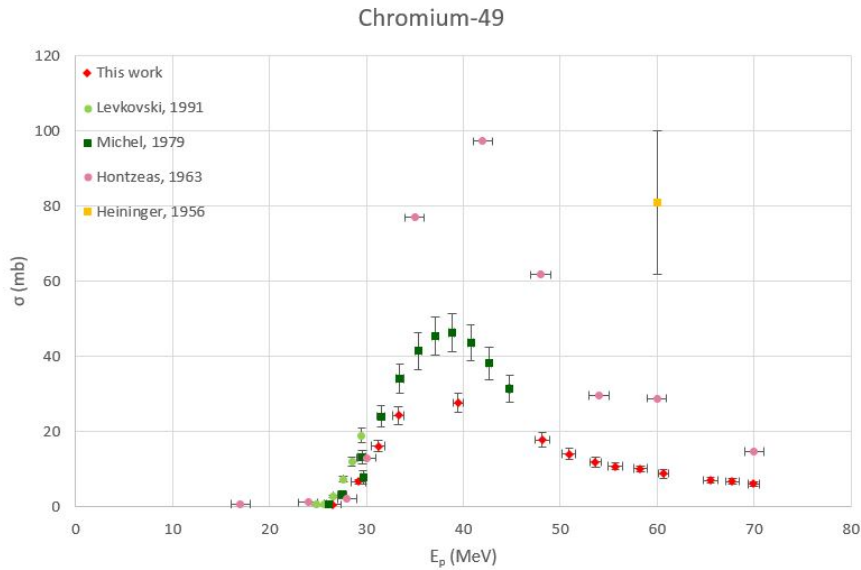


Figure 5.14: Experimental activation cross section results and literature values for ${}^{nat}\text{V}(p,x){}^{49}\text{Cr}$ reactions.

a precise measure of ${}^{49}\text{Sc}$.

The ${}^{51}\text{Cr}$ production has several experimental data available for the comparison, especially at low energies as can be seen in figure 5.15. The data of the first experiments, namely Hontzeas and Albouy [27], differ significantly from the global trend of the other groups results. The dark blue points of Gadioli et al. [28], without any type of uncertainty, reflect the general distribution but they slightly overestimate this work results. The newest data published by Michel et al. (1979), Levkonskij and Detrói et al. are overall in agreement with this work.

As shown in figure 5.16, the ${}^{48}\text{V}$ cross section measured by Detrói is entirely in agreement with the results obtained in this work and also the earlier literature data of Heiniger and Michel (1979) show a good accordance. Instead the agreement with the data of Hontzeas is less good even if the trend is similar.

As anticipated, ${}^{43}\text{Sc}$ production is a particular case. All the previous data deviate significantly from results of this work. Looking at figure 5.17, while Hontzeas et al. found a similar trend but with an early rise of the values, probably due to the use of old nuclear data and monitor reactions, the Detrói group laid out a completely different values distribution. The reason is probably the lack of correction of the ${}^{43}\text{K}$ interference in the 372 keV spectrum γ -peak. In this work, a suitable value to be compared to the

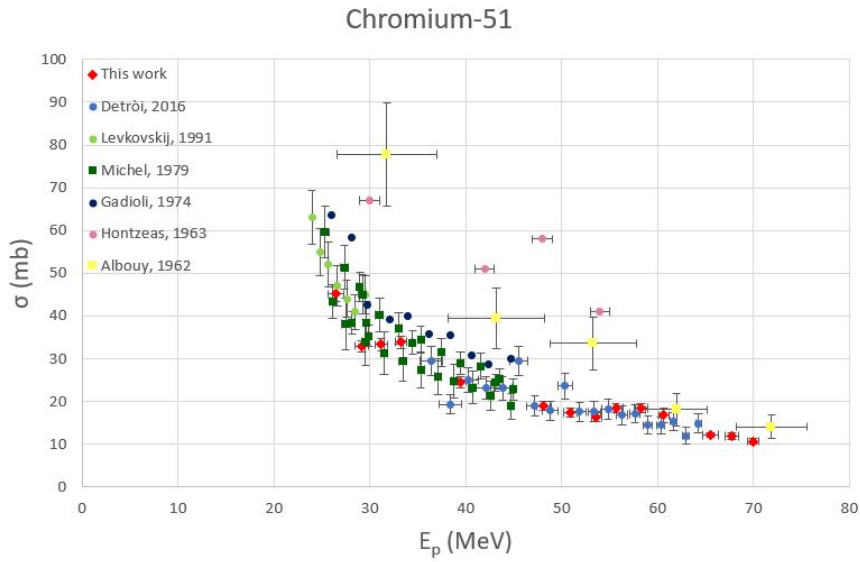


Figure 5.15: Experimental activation cross section results and literature values for $^{nat}\text{V}(p,x)^{51}\text{Cr}$ reactions.

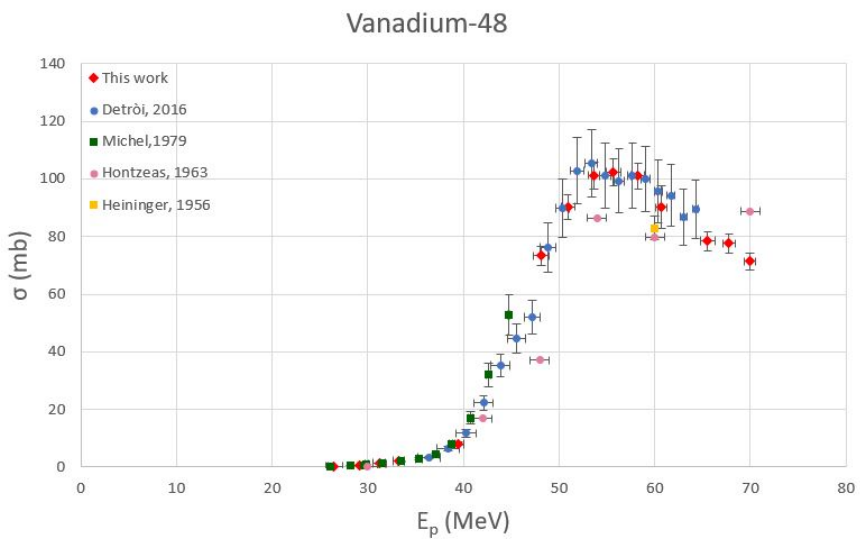


Figure 5.16: Experimental activation cross section results and literature values for $^{nat}\text{V}(p,x)^{48}\text{V}$ reactions.

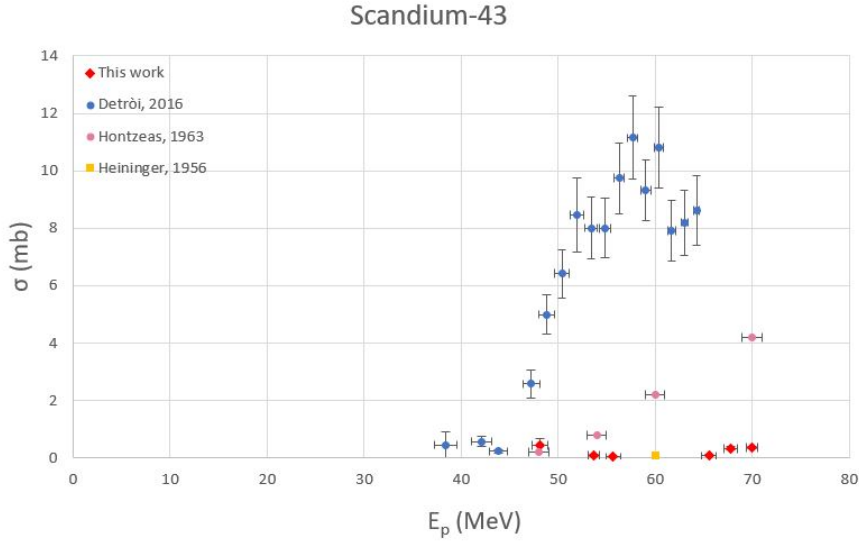


Figure 5.17: Experimental activation cross section results and literature values for ${}^{nat}\text{V}(p,x){}^{43}\text{Sc}$ reactions.

Heininger one is not found. However, this latter differ significantly from the other literature data.

The trends of literature data for ${}^{44m}\text{Sc}$ production cross sections support this work results as shown in figure 5.18. At low energies there is a better agreement with the data from Detrói and Hontzeas while at energies above 60 MeV there is agreement within the errors with the data from Michel (1979).

For the ${}^{44g}\text{Sc}$ case the EXFOR database offers few literature results. This is probably because this isotope cross section needs an elaborated correction due to the isomeric transition from the metastable state, as described in the previous chapter. The trend situation is analogous to ${}^{44m}\text{Sc}$, in fact the plot in figure 5.19 shows a general good agreement between this work results and Detrói and Hontzeas data.

On the contrary, ${}^{46}\text{Sc}$ has a really reach library of previous conducted experiments of cross section measurements. From figure 5.20 it is possible to note that the trend is well described, in fact all the most recent publications, from Detrói and two from Michel (1979) and (1985) [29], are in agreement with results presented in this work. At the same time the oldest data differs markedly (Hontzeas and Heininger). The Hontzeas et al. distribution in particular shows a maximum shifted towards higher energies (of about 10 MeV) followed by a steeper decrease. The Heininger point at 60 MeV has a really large uncertainty but nevertheless it is not compatible with newest data. Anyway it is consistent with Hontzeas measurements.

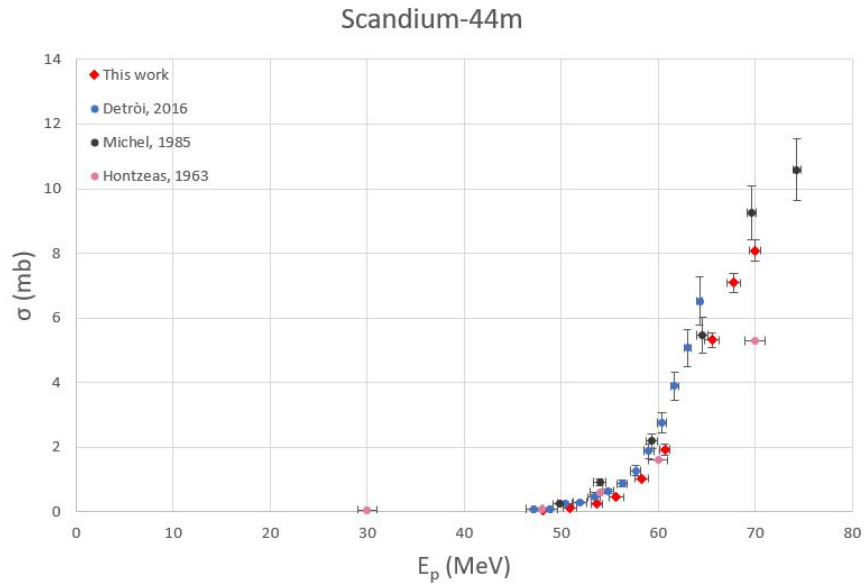


Figure 5.18: Experimental activation cross section results and literature values for $^{nat}\text{V}(p,x)^{44m}\text{Sc}$ reactions.

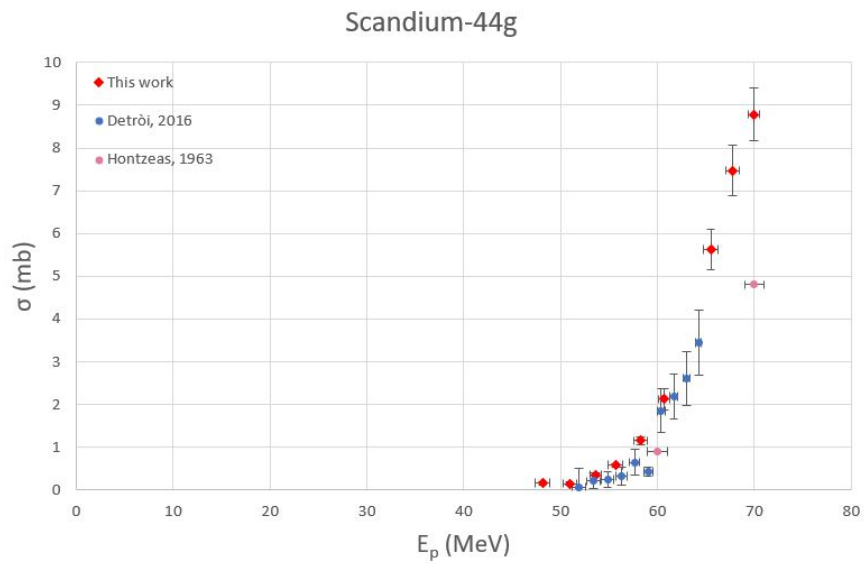


Figure 5.19: Experimental activation cross section results and literature values for $^{nat}\text{V}(p,x)^{44g}\text{Sc}$ reactions.

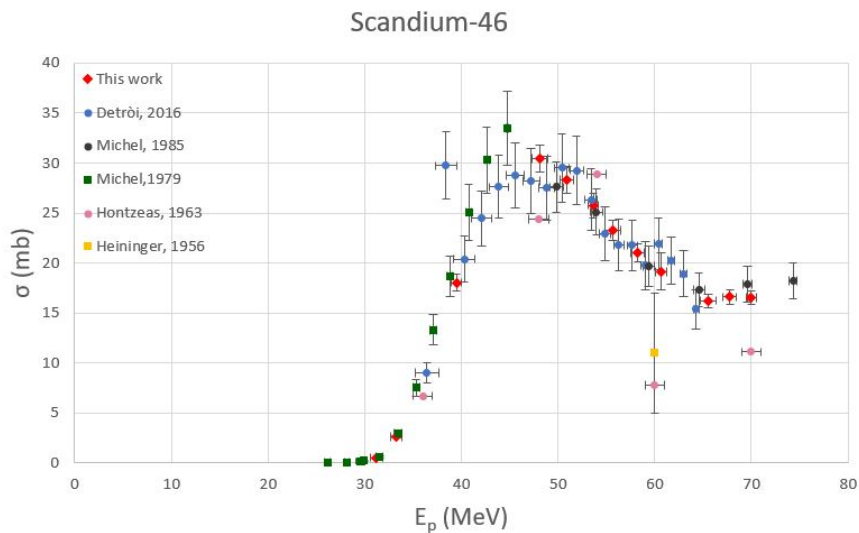


Figure 5.20: Experimental activation cross section results and literature values for $^{nat}\text{V}(p,x)^{46}\text{Sc}$ reactions.

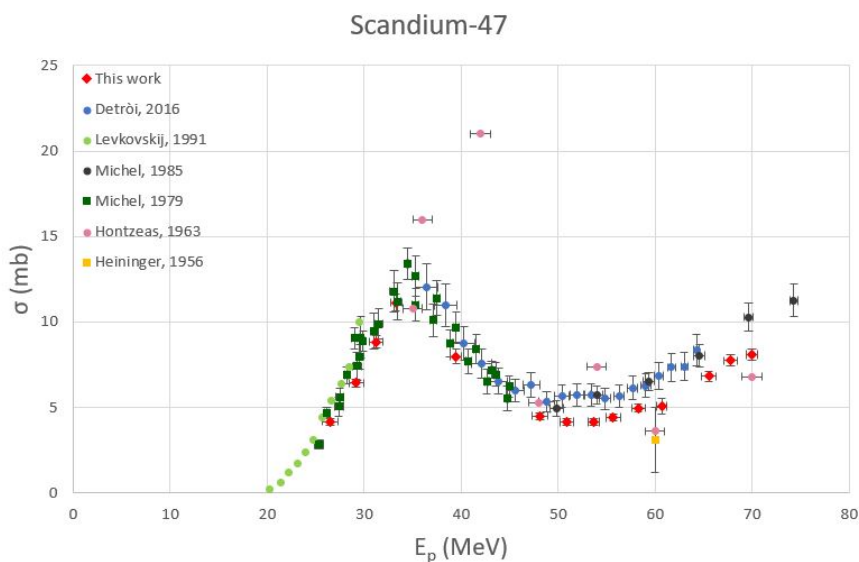


Figure 5.21: Experimental activation cross section results and literature values for $^{nat}\text{V}(p,x)^{47}\text{Sc}$ reactions.

Another isotope with plenty of previous results is ^{47}Sc . The latest data trend agrees with the cross section measured in this work as presented in figure 5.21. At lower energies the agreement is encountered with results from Lewkonskij and Michel (1979). As energy increases, also the data from Detrói and Michel (1985) reflect the trend of this work but the values are a little higher. The older result from Hontzeas simulates the trend of all the others but shifted at higher values both of energy and cross section. The Heininger point at 60 MeV is also reported; this, thanks to its large uncertainty, appears coherent with this work.

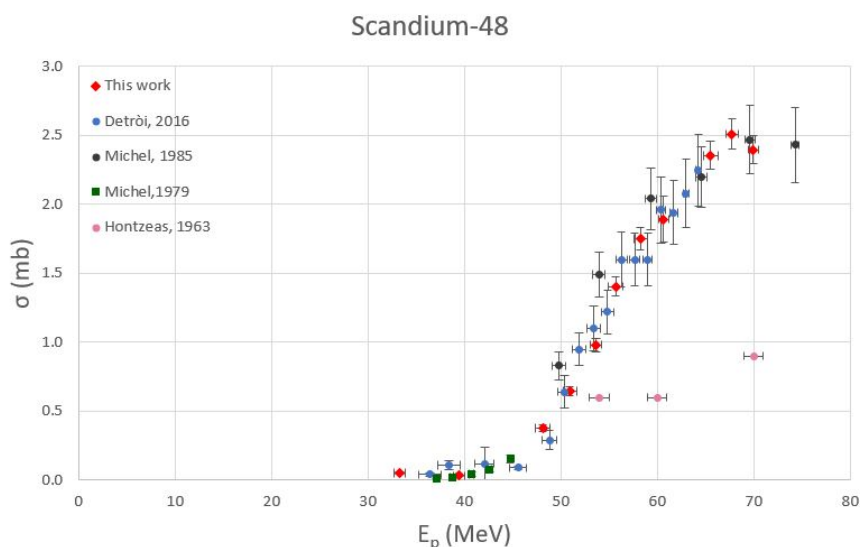


Figure 5.22: Experimental activation cross section results and literature values for $^{nat}\text{V}(p,x)^{48}\text{Sc}$ reactions.

Figure 5.22 shows the results for ^{48}Sc production. It can be clearly noted an agreement in the trend between the data from Detrói, Michel (1979), Michel (1985) and results obtained with this work. On the other hand the old Hontzeas results are significantly different from all the others in the entire energy range.

The literature data for ^{42}K are reported in figure 5.23. Both Heininger and Hontzeas groups presented a single value in the measured energy range, at 60 MeV. Their single old value are significantly low in both cases, approximately about 80% lower than values obtained in this work and by Detrói et al. The data from Michel (1985) are in agreement with this work at energies above 60 MeV, while below 60 MeV values are noticeably higher. Detrói data are perfectly within the experimental errors except for the point at 63 MeV which deviates from this work cross section trend.

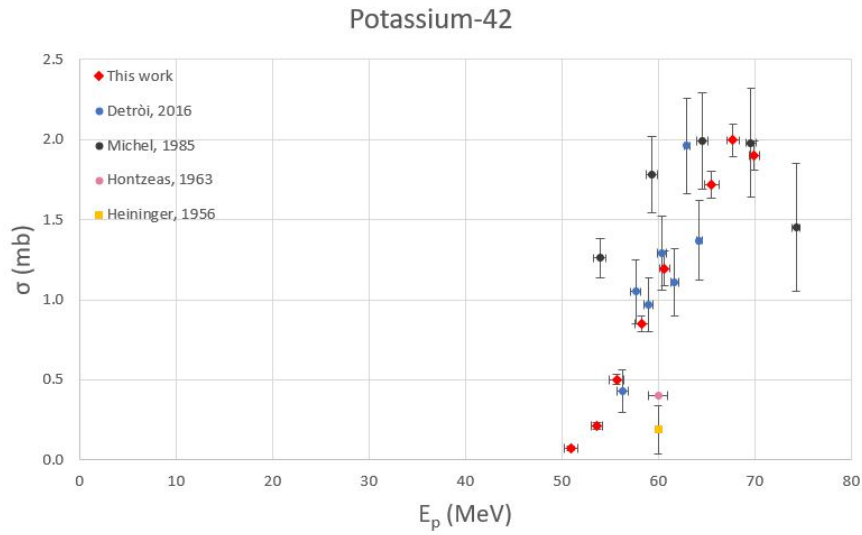


Figure 5.23: Experimental activation cross section results and literature values for $^{nat}\text{V}(p,x)^{42}\text{K}$ reactions.

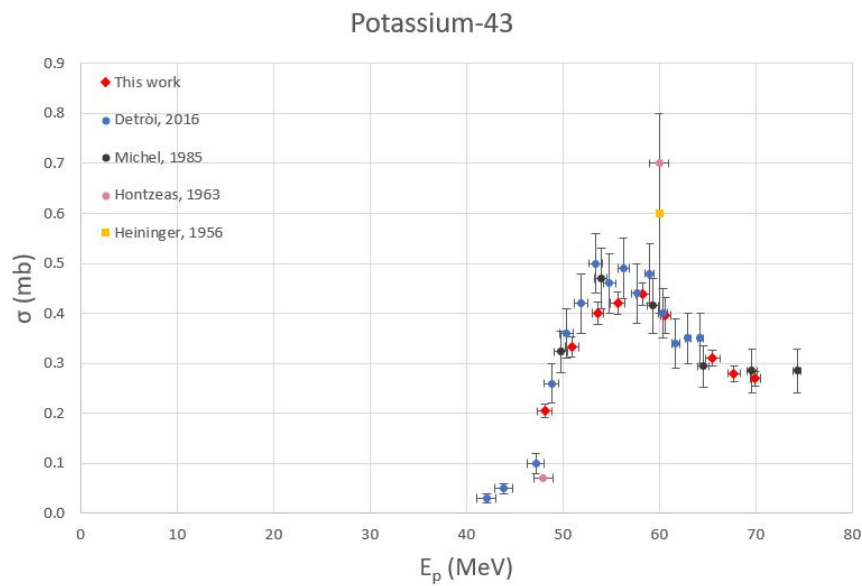


Figure 5.24: Experimental activation cross section results and literature values for $^{nat}\text{V}(p,x)^{43}\text{K}$ reactions.

In the last figure (fig. 5.24) are reported the literature data and results for ^{43}K production. The Detrói ad Michel (1985) data follow totally the trend of this work data all over the investigated energy range. Both the oldest 60 MeV values from Heininger and Hontzeas are too high but the large uncertainty of the Heininger one makes it compatible. Below 48 MeV only the data published by Detrói et al. are available on the international database EXFOR [22].

For medical applications the most important results concerns the identification of an energy range ($E_p < 30$ MeV) where there is not contamination of the co-produced ^{46}Sc in the production of the theranostic radionuclide ^{47}Sc . Enlarging this energy interval up to 35 MeV, it is possible to increase the ^{47}Sc production but, this time, with a contamination of ^{46}Sc . Depending on the irradiation time, this contribution may be considered negligible. However, only further studies on dosimetry on specific radiopharmaceutical biodistribution will impose the maximum limit acceptable for ^{46}Sc contamination.

Another important result is constituted by the ^{43}Sc measured cross section. This thesis work shows clearly different results if compared with previous data. The disagreement is due to the lack of correction of the ^{43}K contribution to the 373 keV γ -line, especially in Detrói et al. data.

In general, in this thesis work, there is the advantage to have uncertainties smaller than in the previous data. This is a consequence of acquiring several γ -spectra for each target foil and of performing a weighted average of the cross section values obtained from each spectrum.

Conclusions

In this thesis work the data analysis and results obtained in the context of the PASTA project are described. The goal was to investigate the possible production of the emerging theranostic radionuclide ^{47}Sc , by using proton cyclotrons and ^{nat}V targets. Considering the medical application of ^{47}Sc -labeled radiopharmaceuticals, particular attention was also given to the measurement of all the co-produced contaminants, especially ^{46}Sc . The experiments (irradiation runs and γ -spectrometry acquisitions) were carried out at the ARRONAX facility, while data analysis for cross section calculation was performed at the INFN-LNL.

Thanks to the several γ -spectrometry acquisitions performed, the decay of the radionuclides of interest can be followed, avoiding possible interferences among the different γ -rays. Moreover, the cross section values resulting from this work have smaller uncertainty values than previous published data.

The results obtained at the end of the analysis of the spectra appear interesting: the need of a pure ^{47}Sc production region can be identified. Among all the cross sections of the reactions $^{nat}\text{V}(\text{p},\text{x})$ measured in this work, $^{nat}\text{V}(\text{p},\text{x})^{47}\text{Sc}$ and $^{nat}\text{V}(\text{p},\text{x})^{46}\text{Sc}$ are the key ones. In fact, ^{46}Sc represents the most dangerous ^{47}Sc contaminant, as all Sc-isotopes it can not be removed from the sample through a chemical separation; in addition it is useless to wait the disappearance of ^{46}Sc after a reasonable interval of time, because ^{46}Sc ($T_{1/2}=83.79$ d) has a half-life longer than ^{47}Sc ($T_{1/2}=3.3492$ h). The comparison of the $^{nat}\text{V}(\text{p},\text{x})^{47}\text{Sc}$ and $^{nat}\text{V}(\text{p},\text{x})^{46}\text{Sc}$ cross section trends allows to determine an energy window, $E_p < 30$ MeV, where ^{47}Sc is produced with almost no contamination of ^{46}Sc . Those results are, at this moment, submitted to the *Journal of Radioanalytical and Nuclear Chemistry*. The submitted article describes the measurements performed and compares the experimental values obtained with some theoretical calculations. An estimation of ^{47}Sc production is also given: in the 26-30 MeV energy range, the ^{47}Sc yield results to be 31 MBq/ μA and 82 MBq/ μA , respectively for 24 h and 80 h of irradiation. In the same energy range the coproduction of ^{46}Sc can be considered negligible, since the corresponding values are 0.01 MBq/ μA and

0.03 MBq/ μ A [30]. This positive result is promising for medicine applications and it provides an interesting energy interval exploitable to obtain ^{47}Sc from a low cost and easy available material, as natural Vanadium can be, for preclinical investigations.

The other remarkable result obtained in this work concerns ^{43}Sc . The novelty arises in the comparison with the literature data. From this work it resulted a suppression of the $^{nat}\text{V}(p,x)^{43}\text{Sc}$ reaction cross section not observed in previous results. The difference with Detrói data may be due to the lack of correction at the 373 keV peak for the ^{43}K contribution. The lack of correction can cause this discrepancy, which is observed also in comparison with the theoretical cross section calculations by Detrói et al. in their article [21]. In particular Detrói outlined how the theoretical prediction underestimates his results. The theoretical evaluations performed with the PASTA project, on the other hand, are in agreement with the experimental values; more details can be found in the submitted article [31]. The oldest data from Hotzeas and Yaffe, instead, have a trend similar to this work results but with a overestimation in the entire energy range. Those results are deduced after a chemical separation process, so there is no more interference of ^{43}K in 373 keV γ line. The overestimation can be explained through the old nuclear data used in 1963.

In conclusion, the production of ^{47}Sc through proton-induced reactions on ^{nat}V target seems to be feasible, with good results in low energy range, at least for precinical studies, since this way of production is economically convenient. For possible future medical applications, in the theranostics field, targets and reactions with an higher yield, but also with higher material costs, may be investigated.

Appendix A

In this appendix are reported the IAEA recommended cross sections used in this work as a reference in the calculation of the cross sections of the radioisotopes produced in a ^{nat}V target bombarded by a proton beam. The data are updated at August 2017 [18]. In figure A.1 are reported the cross section values for the production of ^{24}Na , while in figure A.2 are represented the cross section values for the production of ^{57}Ni .

Observing the trend of those two cross sections, it is possible to clearly understand why the $^{27}\text{Al}(p,x)^{24}\text{Na}$ reaction was chosen for the first three irradiation runs, where the initial proton beam energy was higher than 40 MeV, while in the last three irradiation runs was exploited the $^{nat}\text{Ni}(p,x)^{57}\text{Ni}$ reaction, since the energy was below 40 MeV. It was no longer possible to use the ^{24}Na cross section values at lower energies because ^{24}Na is not produced.

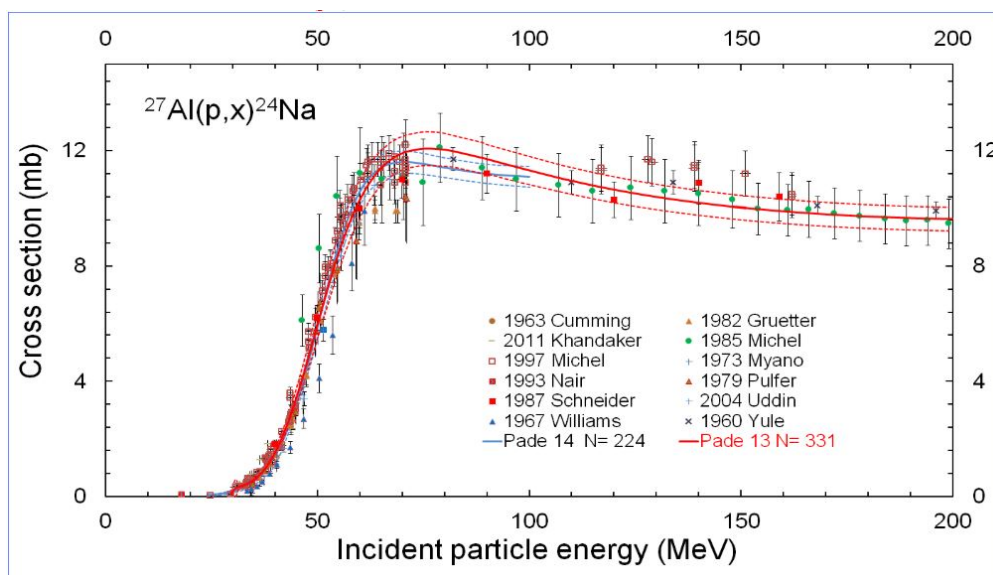


Figure A.1: Recommended cross sections for $^{27}\text{Al}(p,x)^{24}\text{Na}$ reaction with estimated uncertainties, used in the first three irradiation runs [32].

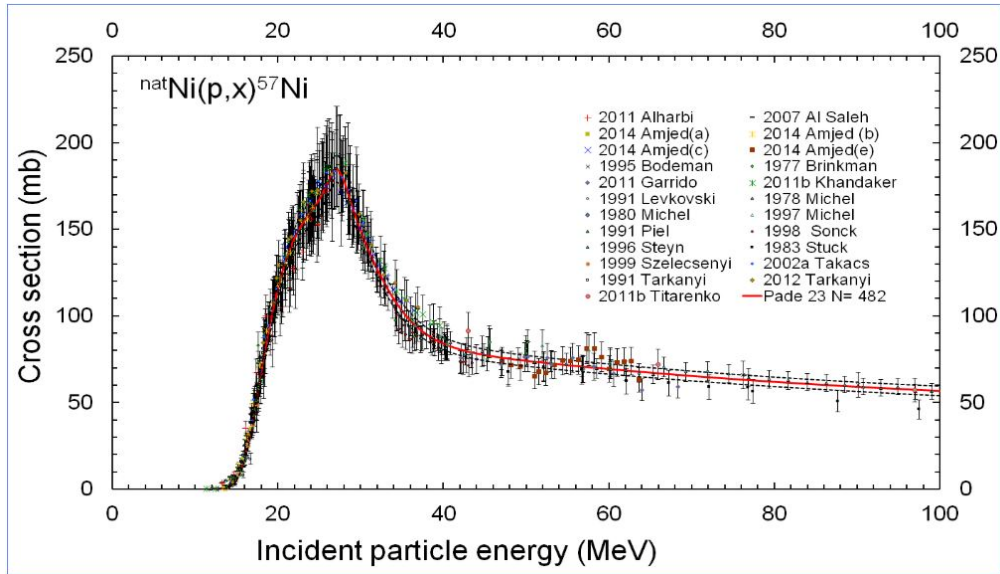


Figure A.2: Recommended cross sections for ${}^{nat}\text{Ni}(p,x){}^{57}\text{Ni}$ reaction with estimated uncertainties, used in the last three irradiation runs [33].

The recommended values are represented by the red solid line. The experimental points are the data collected by different groups. The dashed red line, instead, is the error associated to the fit.

IAEA provides those values, graphically represented, also tabulated [18].

Appendix B

In this appendix are reported all the nuclear reactions induced in a ^{nat}V target by a proton beam energy in the range investigated (26-70 MeV), together with their relative energy thresholds. The data are extracted from the National Nuclear Data Center [17].

Table 5.13: Possible $^{nat}\text{V}(\text{p},\text{x})$ reaction channel available in the energy range investigated [17].

Radioisotope	^{nat}V component	reaction	E_{th} (MeV)
^{48}Cr	^{51}V	$^{51}\text{V}(\text{p},4\text{n})^{48}\text{Cr}$	35.058
	^{50}V	$^{50}\text{V}(\text{p},3\text{n})^{48}\text{Cr}$	23.798
^{49}Cr	^{51}V	$^{51}\text{V}(\text{p},3\text{n})^{49}\text{Cr}$	24.266
	^{50}V	$^{50}\text{V}(\text{p},2\text{n})^{49}\text{Cr}$	13.001
^{51}Cr	^{51}V	$^{51}\text{V}(\text{p},\text{n})^{51}\text{Cr}$	1.565
	^{50}V	$^{50}\text{V}(\text{p},\gamma)^{51}\text{Cr}$	0
^{48}V	^{51}V	$^{51}\text{V}(\text{p},\text{nt})^{48}\text{V}$	23.922
		$^{51}\text{V}(\text{p},\text{d}2\text{n})^{48}\text{V}$	30.303
		$^{51}\text{V}(\text{p},\text{p}3\text{n})^{48}\text{V}$	32.571
	^{50}V	$^{50}\text{V}(\text{p},\text{t})^{48}\text{V}$	12.657
		$^{50}\text{V}(\text{p},\text{dn})^{48}\text{V}$	19.041
		$^{50}\text{V}(\text{p},\text{p}2\text{n})^{48}\text{V}$	21.310
		$^{50}\text{V}(\text{p},\text{d}2\text{n})^{48}\text{V}$	21.310
^{43}Sc	^{51}V	$^{51}\text{V}(\text{p},\text{t}\alpha 2\text{n})^{43}\text{Sc}$	43.080
		$^{51}\text{V}(\text{p},\text{d}\alpha 3\text{n})^{43}\text{Sc}$	49.461
	^{50}V	$^{50}\text{V}(\text{p},\text{t}\alpha \text{n})^{43}\text{Sc}$	31.822
		$^{50}\text{V}(\text{p},\text{d}\alpha 2\text{n})^{43}\text{Sc}$	38.206
		$^{50}\text{V}(\text{p},\text{p}\alpha 3\text{n})^{43}\text{Sc}$	40.475
		$^{50}\text{V}(\text{p},\text{d}2\text{t})^{43}\text{Sc}$	49.766

Radioisotope	<i>nat</i> V component	reaction	E_{th} (MeV)		
^{44}Sc	^{51}V	$^{51}\text{V}(p,t\alpha n)^{44}\text{Sc}$	33.189		
		$^{51}\text{V}(p,d\alpha 2n)^{44}\text{Sc}$	39.570		
		$^{51}\text{V}(p,p\alpha 3n)^{44}\text{Sc}$	41.838		
	^{50}V	$^{50}\text{V}(p,t\alpha)^{44}\text{Sc}$	21.927		
		$^{50}\text{V}(p,d\alpha n)^{44}\text{Sc}$	28.311		
		$^{50}\text{V}(p,p\alpha 2n)^{44}\text{Sc}$	30.580		
		$^{50}\text{V}(p,p2t)^{44}\text{Sc}$	42.141		
		$^{50}\text{V}(p,^3\text{He}tn)^{44}\text{Sc}$	42.920		
		$^{50}\text{V}(p,2dt)^{44}\text{Sc}$	46.255		
		$^{50}\text{V}(p,pdtn)^{44}\text{Sc}$	48.524		
		$^{50}\text{V}(p,^3\text{He}d2n)^{44}\text{Sc}$	49.304		
		^{46}Sc	^{51}V	$^{51}\text{V}(p,d\alpha)^{46}\text{Sc}$	19.084
				$^{51}\text{V}(p,p\alpha n)^{46}\text{Sc}$	21.353
				$^{51}\text{V}(p,t^3\text{He})^{46}\text{Sc}$	33.688
$^{51}\text{V}(p,pdt)^{46}\text{Sc}$	39.290				
$^{51}\text{V}(p,d^3\text{He}n)^{46}\text{Sc}$	40.069				
$^{51}\text{V}(p,t2pn)^{46}\text{Sc}$	41.559				
$^{51}\text{V}(p,p^3\text{He}2n)^{46}\text{Sc}$	42.337				
$^{51}\text{V}(p,3d)^{46}\text{Sc}$	43.403				
$^{51}\text{V}(p,p2dn)^{46}\text{Sc}$	45.671				
$^{51}\text{V}(p,2pd2n)^{46}\text{Sc}$	47.940				
^{50}V	$^{50}\text{V}(p,p\alpha)^{46}\text{Sc}$			10.087	
	$^{50}\text{V}(p,d^3\text{He})^{46}\text{Sc}$		28.810		
	$^{50}\text{V}(p,2pt)^{46}\text{Sc}$		30.301		
^{47}Sc	^{51}V		$^{50}\text{V}(p,p^3\text{He}n)^{46}\text{Sc}$	31.080	
		$^{50}\text{V}(p,p2d)^{46}\text{Sc}$	34.415		
		$^{50}\text{V}(p,2pdn)^{46}\text{Sc}$	36.684		
		$^{50}\text{V}(p,3p2n)^{46}\text{Sc}$	38.954		
		$^{51}\text{V}(p,p\alpha)^{47}\text{Sc}$	10.496		
		$^{51}\text{V}(p,d^3\text{He})^{47}\text{Sc}$	29.212		
		$^{51}\text{V}(p,2pt)^{47}\text{Sc}$	30.701		
		$^{51}\text{V}(p,p^3\text{He}n)^{47}\text{Sc}$	31.480		
		$^{51}\text{V}(p,p2d)^{47}\text{Sc}$	34.814		
		$^{51}\text{V}(p,2pdn)^{47}\text{Sc}$	37.082		
		$^{51}\text{V}(p,3p2n)^{47}\text{Sc}$	39.351		
	^{50}V	$^{50}\text{V}(p,p^3\text{He})^{47}\text{Sc}$	20.218		
		$^{50}\text{V}(p,2pd)^{47}\text{Sc}$	25.823		
		$^{50}\text{V}(p,3pn)^{47}\text{Sc}$	28.092		

Radioisotope	<i>nat</i> V component	reaction	E_{th} (MeV)	
^{48}Sc	^{51}V	$^{51}\text{V}(\text{p},\text{p}^3\text{He})^{48}\text{Sc}$	23.079	
		$^{51}\text{V}(\text{p},2\text{pd})^{48}\text{Sc}$	28.681	
		$^{51}\text{V}(\text{p},3\text{pn})^{48}\text{Sc}$	30.950	
^{42}K	^{50}V	$^{50}\text{V}(\text{p},3\text{p})^{48}\text{Sc}$	19.687	
	^{51}V	$^{51}\text{V}(\text{p},\text{d}2\alpha)^{42}\text{K}$	28.430	
		$^{51}\text{V}(\text{p},\text{p}2\alpha\text{n})^{42}\text{K}$	30.698	
		$^{51}\text{V}(\text{p},\alpha\text{t}^3\text{He})^{42}\text{K}$	43.033	
		$^{51}\text{V}(\text{p},\text{pdt}\alpha)^{42}\text{K}$	48.635	
		$^{51}\text{V}(\text{p},\text{d}^3\text{He}\alpha\text{n})^{42}\text{K}$	49.414	
		^{50}V	$^{50}\text{V}(\text{p},\text{p}2\alpha)^{42}\text{K}$	19.436
	^{50}V	$^{50}\text{V}(\text{p},\text{d}^3\text{He}\alpha)^{42}\text{K}$	38.159	
		$^{50}\text{V}(\text{p},2\text{pt}\alpha)^{42}\text{K}$	39.650	
		$^{50}\text{V}(\text{p},\text{p}^3\text{He}\alpha\text{n})^{42}\text{K}$	40.429	
		$^{50}\text{V}(\text{p},2\text{dp}\alpha)^{42}\text{K}$	43.764	
		$^{50}\text{V}(\text{p},2\text{pd}\alpha\text{n})^{42}\text{K}$	46.033	
$^{50}\text{V}(\text{p},3\text{p}\alpha 2\text{n})^{42}\text{K}$		48.303		
^{43}K	^{51}V	$^{51}\text{V}(\text{p},\text{p}2\alpha)^{43}\text{K}$	20.883	
		$^{51}\text{V}(\text{p},\text{d}^3\text{He}\alpha)^{43}\text{K}$	39.599	
		$^{51}\text{V}(\text{p},2\text{pt}\alpha)^{43}\text{K}$	41.089	
		$^{51}\text{V}(\text{p},\text{p}^3\text{He}\alpha\text{n})^{43}\text{K}$	41.868	
		$^{51}\text{V}(\text{p},\text{p}2\text{d}\alpha)^{43}\text{K}$	45.201	
		$^{51}\text{V}(\text{p},2\text{pd}\alpha)^{43}\text{K}$	47.470	
		$^{51}\text{V}(\text{p},3\text{p}\alpha 2\text{n})^{43}\text{K}$	49.739	
		^{50}V	$^{50}\text{V}(\text{p},\text{p}^3\text{He}\alpha)^{43}\text{K}$	30.610
			$^{50}\text{V}(\text{p},2\text{pd}\alpha)^{43}\text{K}$	36.214
	$^{50}\text{V}(\text{p},3\text{p}\alpha\text{n})^{43}\text{K}$		38.484	
	$^{50}\text{V}(\text{p},\text{d}2^3\text{He})^{43}\text{K}$		49.333	

Bibliography

- [1] IAEA Coordinated Research Project (CRP), *Therapeutic Radio pharmaceuticals Labelled with New Emerging Radionuclides (^{67}Cu , ^{186}Re , ^{47}Sc)*.
- [2] J. Esposito, D. Bettoni, A. Boschi, M. Calderolla, S. Cisternino, G. Fiorentini, G. Keppel, P. Martini, M. Maggiore, L. Mou, M. Pasquali, L. Pranovi, G. Pupillo, C. Rossi Alvarez, L. Sarchiapone, G. Sciacca, H. Skliarova, P. Favaron, A. Lombardi, P. Antonini, A. Duatti, *LARAMED: A Laboratory for Radioisotopes of Medical Interest*, *Molecules* 2019, 24, 20.
- [3] Istituto Nazionale di Fisica Nucleare (INFN), *Selective Production of Exotic Species (SPES)*, <https://web.infn.it/spes/>.
- [4] F. Haddad, L. Ferrer, A. Guertin, T. Carlier, N. Michel, J. Barbet, J. F. Chatal, *ARRONAX, a high-energy and high-intensity cyclotron for nuclear medicine*, *European Journal of Nuclear Medicine and Molecular Imaging* (2008) 35:1377-1387.
- [5] *Perspective in Nuclear Physics*, NuPECC Long Range Plan in NuPECC Publication, 2017, <http://www.nupecc.org/pub/lrp17/lrp2017.pdf>.
- [6] A. Boschi, P. Martini, V. Costa, A. Pagoni, L. Uccelli, *Interdisciplinary Tasks in Cyclotron Production of Radiometals for Medical Applications. The Case of ^{47}Sc as Example*, *Molecules* 2019, 24, 444.
- [7] S. Huclier-Markai, C. Alliot, R. Kerdjoudj, M. Mougin-Degraef, N. Chouin, F. Haddad, *Promising Scandium Radionuclides for Nuclear Medicine: A Review on the Production and Chemistry up to In Vivo Proofs of Concept*, *Cancer Biotherapy and Radiopharmaceuticals*, 2018, Volume 33, Number 8.
- [8] *Nuclear Physics for Medicine*, NuPECC Report in NuPECC Publications, 2014, <http://www.nupecc.org/pub/npm2014.pdf>.

- [9] C. Muller, K. A. Domnanich, C. A. Umbricht, N. P. Van Der Meulen, *Scandium and terbium radionuclides for rdiotheranostics: current state of development towards clinical application*, Br J Radiol 2018; 91: 20180074.
- [10] *Radioisotope production in research reactors*, IAEA, <https://www.iaea.org/topics/radioisotope-production-in-research-reactors>.
- [11] W. R. Leo, *Techniques for Nuclear and Particle Physics Experiments*, 1987, Springer-Verlag.
- [12] J. T. Bushberg, J. A. Seibert, E. M. Leidholdt Jr., J. M. Boone, *The Essential Physics of Medical Imaging*, 2012, Lippincott Williams and Wikins.
- [13] K. Debertin, R. G. Helmer, *Gamma- and X-Ray spectrometry with semiconductor detectors*, 1988, Elsevier Science B. V.
- [14] Kennet S. Krane, *Introductory Nuclear Physics*, 2014, John Wiley and Sons.
- [15] G. Pupillo, *Radioisotopes production via accelerator for nuclear medicine applications*, 2013, PhD diss., Università degli studi di Ferrara.
- [16] G. R. Gilmore, *Practical Gamma-Ray Spectrometry*, 2008, John Wiley and Sons.
- [17] NuDat database 2.7, <http://www.nndc.bnl.gov/>.
- [18] Monitor reactions 2017, https://www-nds.iaea.org/medical/monitor_reactions.html.
- [19] N. Otuka, B. Lalremruata, M. U. Khandaker, A. R. Usman, L. R. M. Punte, *Uncertainty propagation in activation cross section measurements*, Radiation Physics and Chemistry 140 (2017) 502-510.
- [20] J. F. Ziegler, M. D. Ziegler, J. P. Biersack, *SRIM – the stopping and range of ions in matter*, Nuclear Instruments and Methods in Physics Research, B 268 (2010) 1818–1823.
- [21] F. Detrói, F. Tárkányi, S. Takács, A. Hermanne, *Activation cross sections of proton induced reactions on vanadium in the 37-65 MeV energy range*, Nuclear Instruments and Methods in Physics Reaserch B 381 (2016) 16-28.

- [22] EXFOR database, <https://www-nds.iaea.org/exfor/exfor.htm>.
- [23] S. Hontzeas, L. Yaffe, *Interaction on vanadium with protons of energies up to 84 MeV*, Canadian journal of chemistry 41 (1963) 2194-2209.
- [24] C. G. Heining, E. O. Wing, *Spallation of Vanadium with 60-, 100-, 175-, and 240-MeV Protons*, Physcal Review 101 (1956) 1074.
- [25] R. Michel, G. Brinkmann, H. Weigel, W. Herr, *Measurement and Hybrid-Model Analysis of Proton-Induced Reactions with V, Fe and Co*, Nuclear Physics A 322 (1979) 40-60.
- [26] V. N. Levkoskij, *The Cross-Sections of Activation of Nuclides of Middle-Range Mass ($A=40-100$) by Protons and Alpha Particles of Middle Range Energies ($E=10-50$ MeV)*, Act. Cs. By Protons and Alphas, Moscow, 1991.
- [27] G. Albouy, M. Gusakow, N. Poffe, H. Sergolle, L. Valentin, *(P,N)-Reactions at Medium Energy*, Journal de Physique 23 (1962) 1000.
- [28] E. Gadioli, A. M. Grassi Strini, G. Lo Bianco, G. Strini, G. Tagliaferri, *Excitation Function of V-51, Fe-56, Cu-65(P,N) Reactions Between 10 and 45 MeV*, Nuovo Cimento A 22 (1974) 547.
- [29] R. Michel, F. Peiffer, R. Stuck, *Measurement and hybrid model analysis of integralexcitation-functions for proton-induced reactions on vanadium, manganese and cobalt up to 200 MeV*, Nuclear Physics A 441 (1985) 617-639.
- [30] G. Pupillo, A. Boschi, S. Calzaferri, L. Canton, S. Cisternino, L. De Dominicis, A. Duatti, J. Esposito, A. Fontana, F. Haddad, P. Martini, L. Mou, M. Pasquali, H. Skliarova, *Production of ^{47}Sc with natural Vanadium targets: results of the PASTA project*, submitted to Journal of Radioanalytical and Nuclear Chemistry.
- [31] G. Pupillo, L. Mou, F. Haddad, A. Fontana, L. Canton, *^{43}Sc production with proton-induced reaction on Vanadium targets*, submitted to Nuclear Instruments and Methods in Physics Research B.
- [32] $^{27}\text{Al}(p,x)^{24}\text{Na}$ monitor reaction 2017, <https://www-nds.iaea.org/medical/alp24na0.html>.
- [33] $^{nat}\text{Ni}(p,x)^{57}\text{Ni}$ monitor reaction 2017, <https://www-nds.iaea.org/medical/nip57ni0.html>.